Ferroelectric texture of individual barium titanate nanocrystals

Athulya Muraleedharan, Kevin Co, Maxime Vallet, Abdelali Zaki, Fabienne Karolak, Christine Bogicevic, Karen Perronet, Brahim Dkhil, Charles Paillard, Céline Fiorini-Debuisschert, et al.

Ferroelectric texture of individual barium titanate nanocrystals

Athulya Muraleedharan,[†] Kevin Co,[‡] Maxime Vallet,[‡] Abdelali Zaki,[‡] Fabienne Karolak,[‡] Christine Bogicevic,[‡] Karen Perronet,[†] Brahim Dkhil,[‡] Charles Paillard,[‡,¶] Céline Fiorini-Debuisschert,[§] and François Treussart[*,†]

[†]*Université Paris-Saclay, ENS Paris-Saclay, CNRS, CentraleSupélec, LuMIn, 91190 Gif-sur-Yvette, France*

[‡]*Université Paris-Saclay, CentraleSupélec, CNRS, Laboratoire SPMS, 91190 Gif-sur-Yvette, France*

[¶]*Department of Physics, University of Arkansas, Fayetteville AR 72701, USA*

[§]*Université Paris-Saclay, CEA, CNRS, SPEC, 91191 Gif-sur-Yvette, France*

E-mail: francois.treussart@ens-paris-saclay.fr

Abstract

Ferroelectric materials display exotic polarization textures at the nanoscale that could be used to improve the energetic efficiency of electronic components. The vast majority of studies were conducted in two dimensions on thin films, that can be further nanostructured, but very few studies address the situation of individual isolated nanocrystals synthesized in solution, while such structures could open other field of applications. In this work, we experimentally and theoretically studied the polarization texture of ferroelectric barium titanate ($BaTiO_3$, BTO) nanocrystals (NC) attached to a conductive substrate and surrounded by air. We synthesized NC of well defined

quasi-cubic shape and 160 nm average size, that conserve the tetragonal structure of BTO at room temperature.

We then investigated the inverse piezoelectric properties of such pristine individual NC by vector piezoresponse force microscopy (PFM), taking particular care of suppressing electrostatic artifacts. In all the NC studied, we could not detect any vertical PFM signal, and the maps of the lateral response all displayed larger displacement amplitude on the edges with deformations converging toward the center. Using field-phase simulations dedicated to ferroelectric nanostructures, we were able to predict the equilibrium polarization texture. These simulations revealed that the NC core is composed of 180° up and down domains defining the polar axis, that rotate by 90° in the two facets orthogonal to this axis, eventually lying within these planes forming a layer of about 10 nm thickness mainly composed of 180° domains along an edge. From this polarization distribution we predicted the lateral PFM response, that revealed to be in very good qualitative agreement with the experimental observations. This work positions PFM as a relevant tool to evaluate the potential of complex ferroelectric nanostructures to be used as sensors.

Keywords

Ferroelectrics, Barium titanate, Nanocrystal, Piezoresponse force microscopy, Phase field simulation

Introduction

Ferroelectric materials gather a remarkable set of physical properties, including a large dielectric permittivity, a piezoelectric response, and ferroelectric hysteresis that make them vital for several industries.[1] Recently, progress in the synthesis and growth methods of ferroelectrics has allowed new exotic effects to be discovered at low dimensions. For instance, new quasiparticles such as (anti)vortices or polar skyrmions have been widely predicted[2–7]

and subsequently observed[8–12] due to electrostatic depolarization in two-dimensional structures such as superlattices or thin films, or in one-dimensional nanowires embedded in a dielectric matrix. These topological defects are often endowed with rich properties, such as negative dielectric capacitance,[13] an effect envisioned to reduce Field Effect Transistor energy consumption. The polarization texture in 0-dimensional ferroelectric crystals, that is, ferroelectric nanodots and nanocrystals (NC) have been less studied; yet recent (mainly simulation) studies have reported exotic polarization textures in NC as well.[14–17]

Therefore, in this work we set out to understand the polarization texture of ferroelectric $BaTiO_3$ (BTO) NC by an original combination of experiments and phase field modeling.[15] BTO is a prototypical ferroelectric material with a paraelectric phase above 120°C in bulk crystal. Below that transition temperature, and down till about 5°C, a polar order and a tetragonal deformation of the unit cell are established. This is the room temperature ferroelectric phase. Below 5°C, a succession of ferroelectric orthorhombic and rhombohedral phases appears.[18] The synthesis of BTO nanocrystals with well-controlled morphology, size, and properties is well established.[19,20] Compared to bulk, the larger surface-to-volume ratio of BTO NC leads to starkly different properties, particularly ferroelectric ones, which strongly depend on boundary conditions. For instance, the phase transition from the para- to the ferro-electric state is more diffuse in BTO NC.[21] Furthermore, the small dimensions offered in BTO NC, combined with the presence of electrical polarization, offer competitive advantages for charge separation in photovoltaic or photocatalytic applications.[22–28] However, there is little to no report on the nanoscale inhomogeneity of the polarization distributions, which may be critical for applications such as photocatalysis.

A frequently used technique of characterization at the nanoscale is the high-angle annular dark-field (HAADF) imaging mode of scanning transmission electron microscopy (STEM), harnessing its high sensitivity to ion nuclei displacements. A polarization structure was observed by HAADF-STEM within 200 nm sized BTO free-standing cuboids milled in a bulk crystal using a focused ion beam. The observations were interpreted as the results of quadrant

structures of 90° polarization domains.[29] As the nanocuboids were milled in bulk, one cannot exclude that the domain structure is partly induced by the fabrication process, as recently reported.[30] Other electron beam-based techniques, capable of sensing the electric field of the sample via phase accumulation and its subsequent retrieval, are used to probe the local order in nanoferroelectrics.[31] In particular, Polking *et al.* harnessed off-axis electron holography to prove that a 10 nm-sized BTO nanocube retains ferroelectric properties, as evidenced by the presence of an electric field around the NC only below Curie temperature.[32] Moreover, taking advantage of the atomic resolution provided by their aberration-corrected STEM, they were able to reconstruct the atomic displacements in the 10 nm nanocube and demonstrated that it is made of a single ferroelectric domain. Using Bragg coherent X-ray diffraction imaging of single BTO nanoparticles of larger size (160 nm) embedded in a non-ferroelectric polymer matrix, Karpov *et al.*[33] extracted much more complex polarization field (than in 10 nm-sized BTO nanocube) showing that it arranges in a flux-closure manner (forming a vortex), that can be consistently reproduced by phase field simulations. Alternatively to these non-contact methods based on electron or X-ray beams, near field microscopy in contact mode has been used. For example, the ferroelectric properties of an array of 60 nm-sized dots nanostructured in a thin film of bismuth iron oxide grown on a conductive substrate have been explored by Piezoresponse Force Microscopy (PFM),[14] revealing various polarization textures in individual dots.

Here, we combine PFM and phase field simulations to study the polarization texture of isolated BTO nanocubes in their native ferroelectric state, as produced by solvothermal synthesis. We first present NC synthesis and structural characterization, then electromechanical mapping on individual NC using PFM, and finally phase field simulations of such displacement fields. We show that the simulations are in very good qualitative agreement with the PFM data, enlarging the domain of application of PFM, mostly used for thin film characterization, to complex nanostructures, for which phase field simulations can be demanding.

Results and discussion

Barium titanate nanocrystals of quasi-cubic shape

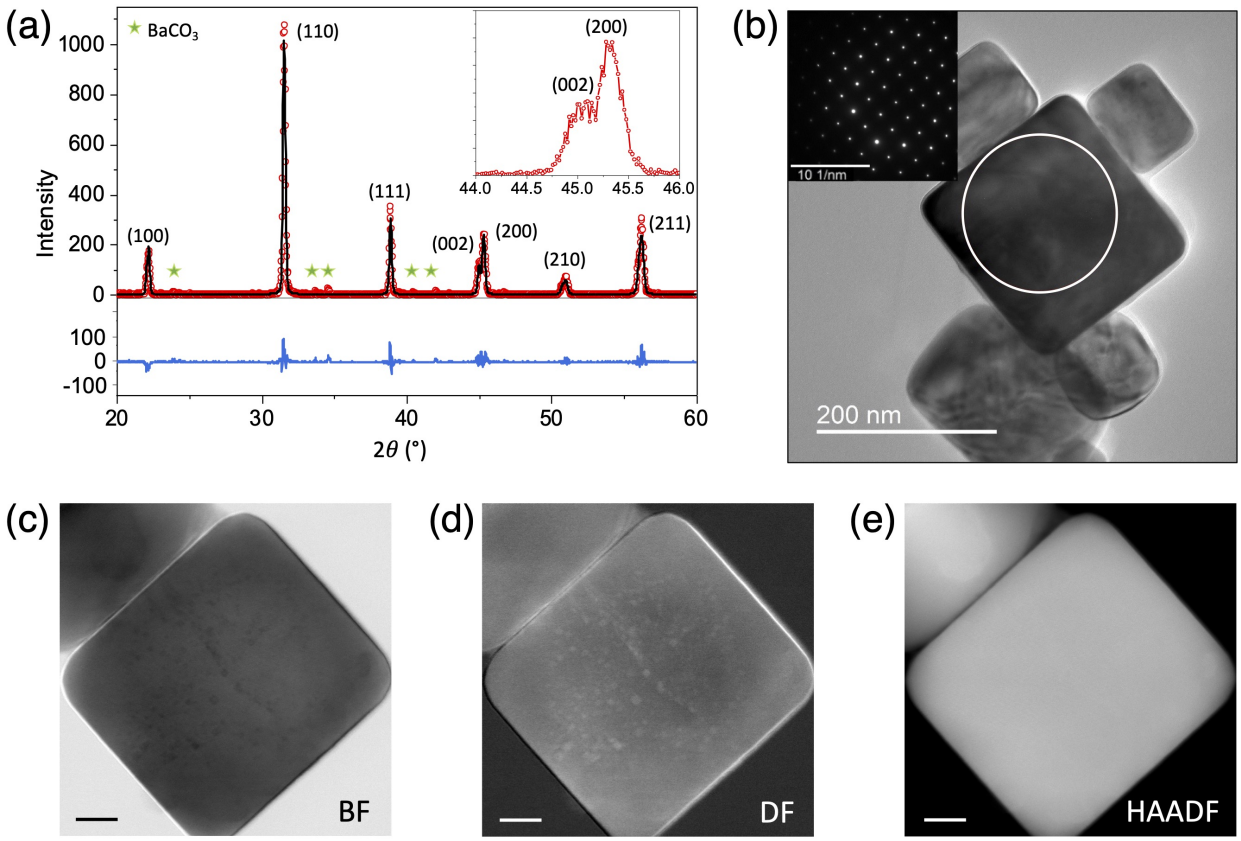

Figure 1: **Structural characterization of barium titanate nanocubes.** (a) X-ray diffractogram showing all the detected peaks indexed to the tetragonal phase of BTO. The data points observed are represented as red circles, and the calculated intensities are shown as a black solid line. The inset graph shows, near $2\theta = 45°$, two separate peaks for (002) and (200) planes evidencing the tetragonal structure. Green stars indicate small peaks associated to the structure of residual $BaCO_3$ crystallites precursor. The solid blue line at the bottom represents the difference between the observed and calculated intensities. (b) TEM image of a small aggregate of nanocrystals. Scale bar: 200 nm. Inset: electron diffraction pattern on the encircled region, consistent with a single-crystal nature. Scale bar: 10 nm^{-1}. (c-e) HR-STEM images of another BTO nanocrystal, in bright-field BF (c), dark-field DF (d) and high-angle annular dark-field HAADF (e) modes. Scale bar: 20 nm. BF and DF modes display multiple square-shaped spots within the NC, which may be little pores.

Quasi-cubic shaped barium titanate nanocrystals were synthesized using the solvothermal method described in Bogicevic *et al.*[19] (Materials and Methods). Supporting Infor-

mation Figure S1a shows a large field-of-view scanning electron microscopy image of the as-produced powder, confirming the overall quasi-cubic shape. We first did a structural analysis of this powder, from which we then prepared the dilute suspension for PFM studies of single nanocrystals.

Figure 1a displays the powder X-ray diffractogram at the temperature of 293 K showing the characteristic peak splitting of tetragonal phase at twice the diffraction angle $2\theta \approx 45°$, corresponding to the $(hk\ell)$ Miller indexes (002) and (200), while a purely cubic phase would have a single peak associated to (002). Rietveld refinement of the diffractogram (Materials and Methods) reveals a well-known tetragonal structure (space group symmetry P4mm) for BTO at room temperature (293 K), with $a = b = 4.0072 \pm 0.0005$ Å and $c = 4.0339 \pm 0.0006$ Å, leading to a lattice parameter ratio $(c/a)_{\mathrm{NC}} = 1.0067 \pm 0.0002$. However, compared to bulk BTO for which $(c/a)_{\mathrm{bulk}} = 1.0101 \pm 0.0002$,[34] the ratio measured in our NC is significantly smaller by 0.3% and closer to one, indicating that its lattice is slightly less tetragonal and more cubic than the bulk one, in agreement with other reports on BTO nanocrystals.[35,36] We also used transmission electron microscopy (TEM, Materials and Methods) to investigate the crystalline structure at the single particle level. Figure 1b shows a TEM image of a small aggregate accompanied with the diffraction pattern of the selected area on the central nanocrystal. The regular pattern obtained is consistent with the monocrystalline nature of the selected NC.

The reduced tetragonality that we observed in BTO nanocrystals compared with the bulk was reported in several studies and was attributed to different sources. Firstly, one study evidenced by high-resolution scanning TEM (HR-STEM) the presence of a thin shell of cubic symmetry at BTO NC surface.[37] This observation was further supported by indirect measurements and models.[36] We examined our BTO NC edge with HR-STEM (see Figure S2) but could not detect a layer of different symmetry. Secondly, we estimated to 0.19% the inhomogeneous strain from Figure 1a diffractogram using Williamson-Hall method with a Cauchy peak profile[38] (see Figure S1b), which is smaller than the value of 0.26% recently

reported,[39] but not negligible. This strain is probably due to hydroxyl groups coming from the barium precursor and remaining inside the nanocrystals as point structural defects. The latter would migrate to the surface only at temperatures much higher than those used during solvothermal synthesis. Other sources of strain are small square-shape pores that we observed in bright-field (Figure 1c) and dark-field HR-STEM (Figure 1d) of one nanocrystal, but not in high-angle annular dark-field which rather shows chemical contrast. In some particles with rounder morphology we even observed much larger pores (see Figure S2c,d). We reported such pores in a previous study on the same sample,[19] and showed evidences that they result from the merging and restructuration, upon temperature increase above 200°C, of nanotori, which are the primary structure formed at low temperature.

As these defects may impact the ferroelectric properties, we further conducted Raman spectroscopy on BTO powder, at temperatures varying between 80 K and 540 K. In the centro-symmetrical paraelectric cubic phase, BTO is Raman inactive, contrary to the tetragonal phase, which symmetry leads to height Raman optical-phonon active modes.[40] We monitored the area variation of the narrowest active Raman peak (305 cm^{-1} wavenumber, at 300 K) with temperature (see Figure S3a), as in Begg *et al.*[41] and observed a marked decrease at 395 ± 2 K (Figure S3b) in agreement with the commonly accepted BTO Curie temperature of 120°C. This observation indicates that, despite a reduced tetragonality compared with the bulk, the BTO NC we synthesized keeps the hallmark of the bulk BTO ferroelectric phase transition. Our objective was then to examine the ferroelectric domain texture of single BTO nanocrystals, and to this aim we performed vector piezoresponse force microscopy.[42]

Piezoresponse displacement measurements

PFM allows nondestructive imaging and control of ferroelectric domains at the nanoscale via bias-induced converse piezoelectric effect mechanical deformations. It has gained interest in helping the development of new nanoferroics.[43,44] The basic principles of PFM are recalled

in Supporting Information Text S1 and for example in ref.[45] PFM is a near-field microscopy operating in contact mode, which makes the study of individual nanocrystals challenging, as they must be firmly immobilized on a conductive substrate, while having their upper surface directly exposed to the conductive tip.

For such a study we prepared a sample with isolated NC attached to a conductive substrate made of indium tin oxide (ITO)-coated coverglass, with a marking grid on top of the coating, to facilitate the correlation between scanning electron microscopy prelocalization of isolated NC and their subsequent study by PFM. The ITO-coated coverglass with the grid is first covered with a thin layer of a conductive polymer (PEDOT:PSS), on top of which a dilute aqueous suspension of the NC is spincoated (Materials and Methods), as displayed on Figure 2a. We optimized the various parameters to achieve a polymer thickness in the range of 40-50 nm (see Figure S4a). Thanks to a good wettability of $BaTiO_3$ by water,[46] the concave meniscus (visible on Figure S4b) forming on the edges of the nanoparticles drags them down by surface tension, and after drying the polymer layer in an oven, about two-thirds of the particle height emerges and can be directly contacted by the PFM conductive tip.

Figure S5a shows a typical low magnification SEM image of the sample with an apparent cell of the numbered grid. To conduct the PFM study, we first selected and located isolated NC, like the one at the center of Figure S5b, and characterized their size distribution, that fell in the range of 120-210 nm, as shown on Figure S6a. Moreover, Figure S6b indicates that about 65% of these NC have an planar aspect ratio larger than 0.95 in the sample plane, which is a good indication of close to perfect cubic shape.

PFM measurements were conducted according to the experimental configuration presented in Figure 2b. We first took care of minimizing artifacts that could stem from electrostatic charge accumulation.[47] We evidenced such parasitic effects when using conventional deflection laser spot setting at the cantilever tip. These effects include the observation on the conductive and nonferroelectric surface of the ITO of an apparent contact resonance of the cantilever (see Figure S7a), an hysteresis loop (Figure S7b), and charge accumula-

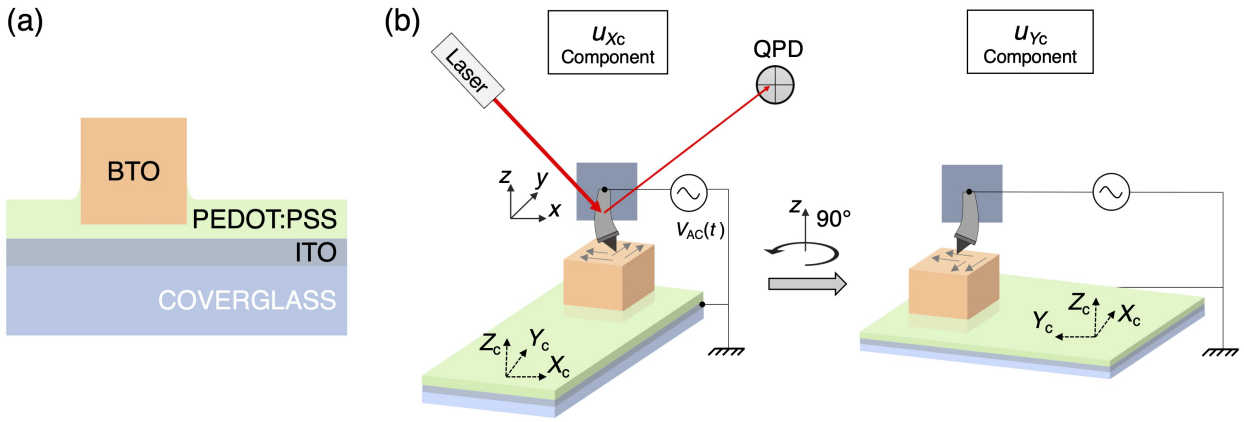

Figure 2: **Experimental configuration of lateral piezoforce response measurement on a single BTO nanocrystal**. (a) Immobilization of BTO NC onto an ITO-coated coverglass with a thin film of PEDOT:PSS conductive polymer. (b) Schematics of lateral PFM measurement. (x, y, z) and (X_c, Y_c, Z_c) are the laboratory and crystal-attached frames, respectively. The measurement consists in applying an AC-voltage $V_{AC}(t) = V_{AC}\cos(2\pi f_d t)$ to the tip, with f_d being the driving frequency, set close to the tip contact resonance, and $V_{AC} = 1.5$ V. The PFM tip, aligned along the y axis, is scanned along the x axis, which is colinear to X_c axis initially (left configuration). During scanning, the nanocrystal in-plane polarization domains (displayed by gray arrows) induce shear displacements of the tip along the x axis, oscillating in phase or out of phase with $V_{AC}(t)$, depending on the orientation of the projection of the polarization along the X_c axis. The resulting displacement amplitude u_{X_c} is inferred from the deflection of the PFM laser as measured by the quadrant photodiode (QPD). To reduce electrostatic artifacts, we set the laser beam to hit the cantilever at the electrostatic blind spot (ESBS, see main text). To access the displacement u_{Y_c} along the Y_c axis, we rotate the sample by 90° counterclockwise around the laboratory z axis, and repeat the scan along the x axis (right configuration; the laser and QPD are not shown for the sake of clarity).

tion in freshly "written" regions (Figure S8a,b). We were able to strongly reduce these non-electromechanical artifacts by implementing the recently published electrostatic blind spot (ESBS) settings[47] as detailed in the Supporting Information Data S2.2 and shown on Figure S7c,d and Figure S8c-f.

Once these parasitic effects were minimized, we could more reliably map the lateral PFM two-dimensional displacement field (LPFM) of the top surface of immobilized NC. As the PFM cantilever scans only along the direction x of the laboratory frame, the sample must be rotated by 90° around the vertical z laboratory axis, as shown on Figure 2b, to acquire the Y_c LPFM component after the X_c one, (X_c, Y_c, Z_c) being a frame of reference attached

to the NC of interest.

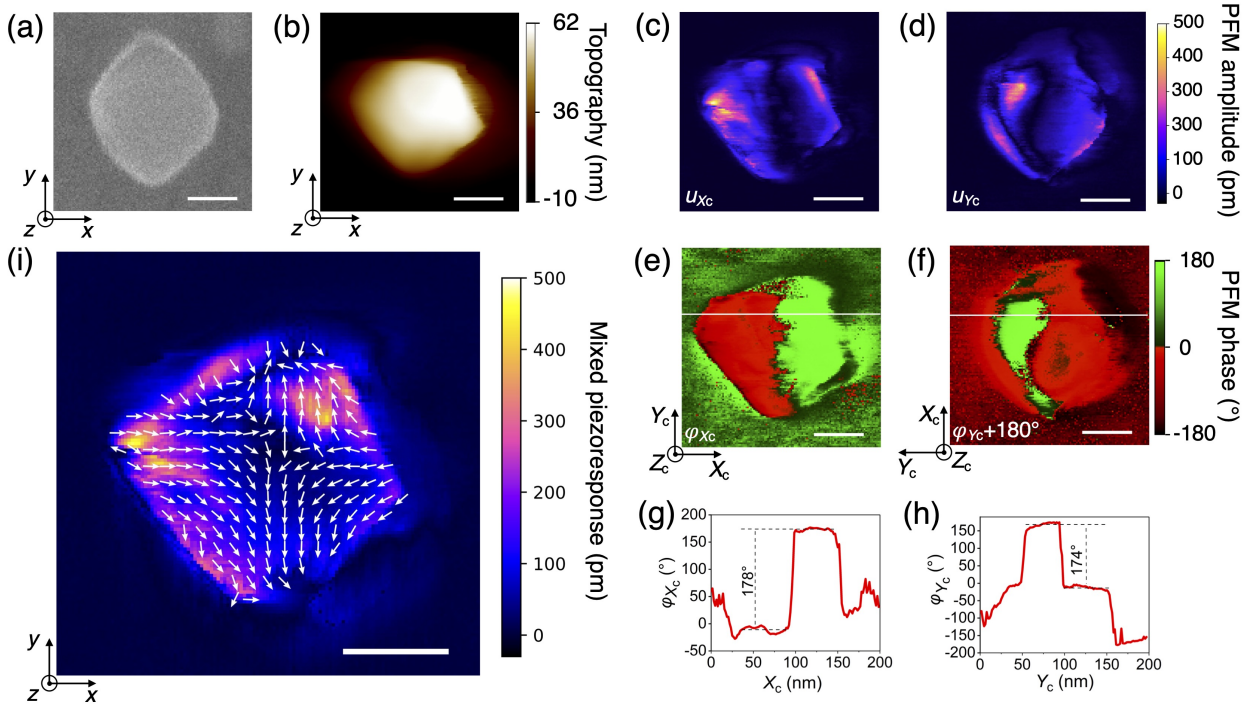

Figure 3: **Lateral piezoresponse displacement mapping on a single BTO NC**. (a) SEM scan of the investigated particle, with an approximately square shape and size of 125 nm. The laboratory frame is denoted (x, y, z), with (Oz) perpendicular to the substrate. We scan the cantilever along the x axis. (b) AFM height measurement (contact mode) of the same BTO NC oriented as shown in (a). (c,d) Amplitudes u_{X_c} and u_{Y_c} of lateral piezoresponses along the X_c and Y_c axis respectively of the frame (X_c, Y_c, Z_c) attached to the nanocrystal and confounded with (x, y, z) before sample rotation. To record u_{Y_c} the sample was rotated 90° counterclockwise around the z axis. The amplitude of the electric field modulation applied was 1.5 V. (e,f) Lateral piezoresponse phase associated to X_c- and Y_c axis respectively. (g,h) Cross sections of the (e) and (f) phase maps. (i) Mixed lateral piezoresponse field $\boldsymbol{u}^{\mathrm{m}}(u_{X_c}\cos(\varphi_{X_c} - \varphi_{\mathrm{offset}}), u_{Y_c}\cos(\varphi_{Y_c} - \varphi_{\mathrm{offset}}))$, displayed by a superimposed norm (color code) and direction maps (array of fixed-length arrows at the nodes of a 7.8 nm pitch grid). Note that the lateral displacement values are not absolute, as we did not perform any calibration. Scale bars (all scans): 50 nm.

We implemented this procedure to map the LPFM of four nanocrystals, setting the voltage modulation amplitude applied to the tip at $V_{\mathrm{AC}} = 1.5$ V for all of them. Figure S9 shows a typical cantilever contact resonance curve, used to set the driving frequency close to its maximum. Figure 3 exemplifies LPFM measurements in one of the four NC, whose lateral dimensions measured using SEM (Figure 3a) are 125 nm $\times$ 125 nm. The height of the

portion of the NC emerging from the PEDOT:PSS layer, as measured by AFM, is ≈ 72 nm (Figure 3b). Assuming a cubic shape, the depth of penetration of the particle in the polymer layer is then ≈ 53 nm, which is consistent with Figure S4a thickness estimate.

Figure 3c-h then display LPFM measurements carried out on this NC, for which the electric field applied by the tip (along the laboratory z axis) has an amplitude $E_z^{\mathrm{exp}} = 120$ kV/cm across the supposedly 125 nm-sized particle. Figure 3c shows a map of u_{X_c}, which is the amplitude of the voltage-induced local lateral deformation along the X_c direction. Figure 3e shows the map of the phase difference φ_{X_c} between V_{AC} applied to the tip and the NC piezoresponse along the X_c direction. To access LPFM measurement along the Y_c direction, the sample was rotated counterclockwise by $90 \pm 2°$, around the laboratory z axis. Figure 3d and Figure 3f show the amplitude u_{Y_c} and phase $(\varphi_{Y_\mathrm{c}} + 180°)$ maps respectively, along the Y_c-direction. Note that the phase actually measured in the rotated-sample orientation is $\varphi_{Y_\mathrm{c}} + 180°$ to account for the fact that the Y_c axis, after rotation, points in the opposite direction of the original X_c axis. We observed a small instrumental phase offset, $\varphi_{\mathrm{offset}} = -10 \pm 2°$, for the in-phase piezoresponse (refer to Materials and Methods for its determination), which we arbitrarily chose to be the phase of the in-phase domain (with a positive X_c component). The cross-sections of Figure 3e,f evidence a phase difference of $\approx 180°$ between the red and green regions, revealing the presence of in-plane electric polarization domains with opposite orientations along the scanning direction.

We finally inferred the mixed lateral piezoresponse displacement field $\boldsymbol{u}^{\mathrm{m}}$ components, defined as $u^{\mathrm{m}}_{X_\mathrm{c}} \equiv u_{X_\mathrm{c}} \cos(\varphi_{X_\mathrm{c}} - \varphi_{\mathrm{offset}})$ and $u^{\mathrm{m}}_{Y_\mathrm{c}} \equiv u_{Y_\mathrm{c}} \cos(\varphi_{Y_\mathrm{c}} - \varphi_{\mathrm{offset}})$, displayed in Figure 3i. We observe that the displacement directions close to the nanocrystal edges are either parallel or orthogonal to these edges, and that these orientations propagate from the surface to the center.

The same behavior was observed for the lateral PFM applied to the three other nanocrystals investigated (see Figures S10 to S12.) The measured lateral responses display non-homogeneous converging deformation fields that reflect complex underlying ferroelectric tex-

tures, and that we further investigated by simulations, as discussed later. Note that similar converging deformation fields were reported in single bismuth iron oxide dots of cylindrical shape, nanostructured as an array in a thin layer.[14]

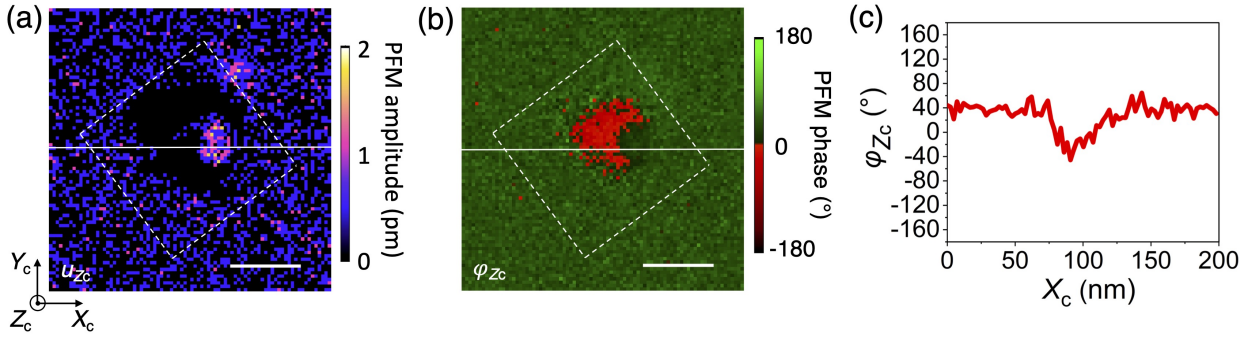

Figure 4: **Vertical piezoresponse of the same nanocrystals as the one of Figure 3, which footprint is marked by the white dashed line square**. (a,b) PFM amplitude (a) and phase (b) maps showing no significant contrast. (c) Cross section of the phase image along the solid white line. Scale bars (all images): 50 nm.

We also measured the vertical piezoresponse (VPFM) that is shown in Figure 4, and detected no significant vertical piezoresponse amplitude compared to the lateral one as $u_{Z_c}^{\max}/u_{X_c}^{\max} \approx 4 \times 10^{-3}$ (Figure 4a). We observe a phase difference of $\approx -80°$ relative to the surrounding, in the exact same region where there is no displacement amplitude at all. We therefore suspect that this phase value has no physical meaning.

In order to interpret these PFM data, we carried out ferroelectric phase field simulations, first without any applied external electric field, to get the equilibrium ferroelectric domain distribution, and then in condition of PFM measurement, with an external applied electric field which amplitude is of the order of magnitude of the one used in the experiment.

Phase field simulations

We considered a cubic-shape BTO nanocrystal of 100 nm size, embedded in air and used the FERRET module[15] of the Multiphysics Object Oriented Simulation Environment (MOOSE), an open-source software maintained by Idaho National Laboratory.[48] FERRET is a finite element implementation of a ferroelectric phase field model, which we utilise here to capture

the polar and elastic equilibrium state of BTO nanocrystals, as well as their response to static electric fields. In the experiment, one facet of the particle is in contact with a conductive medium. However, as shown in Prosandeev and Bellaiche,[49] asymmetric screening with a metal electrode does not destroy the domain structure in ferroelectric thin films, and the simulations conducted probably extend to the experimental case of the bottom facet surface attached to a conductive layer with the rest of the nanocube exposed to air.

Equilibrium domain structure. We first determined the equilibrium polarization and displacement fields, $\boldsymbol{P}^{\rm eq}(\boldsymbol{r})$ and $\boldsymbol{u}^{\rm eq}(\boldsymbol{r})$ by minimising the energy of a BTO nanocube with random and small initial polarization and mechanical displacement field components. Figure 5a shows that minimization of the free energy of the system leads to a multidomain structure consisting of domains polarized upward and downward along the (O$Z_{\rm c}$) axis, which we now refer to as the polar axis [001]. We estimate that the core of the BTO NC made of upward and downward tetragonal domains along (O$Z_{\rm c}$) represents 60% of the fraction of the volume of the NC. From the polarization profiles along lines L_1 and L_2 (Figure 5b,c), we inferred a polarization component amplitude $P_{Z_{\rm c}} = \pm 0.265$ C/m^2 in these up and down domains, which is consistent with what has been measured[50] or calculated[51,52] in the tetragonal ferroelectric phase of barium titanate.

Looking at the domain walls separating up and down domains in Figure 5c polarization profile, we observe that they are mostly of the Ising-type, *i.e.* the transition is accomplished by modulating the $P_{Z_{\rm c}}$ component. We do see, however, that some walls retain partial Bloch characteristics (rotation of the polarization in planes parallel to the domain wall, *i.e.* showing non-vanishing $P_{X_{\rm c}}$ component, for example at $Y_{\rm c}$ =11, 35, 55 and 90 nm) or Néel characteristics (rotation of the polarization in a plane orthogonal to the domain wall, *i.e.* with non-zero $P_{Y_{\rm c}}$, for example at $Y_{\rm c}$ =45 and 55 nm), as schematized on the polarization profile line L_2 in Figure 5d.

Note that, in surface planes along the polar axis like $X_{\rm c} = 0$ nm, the polarization aligns

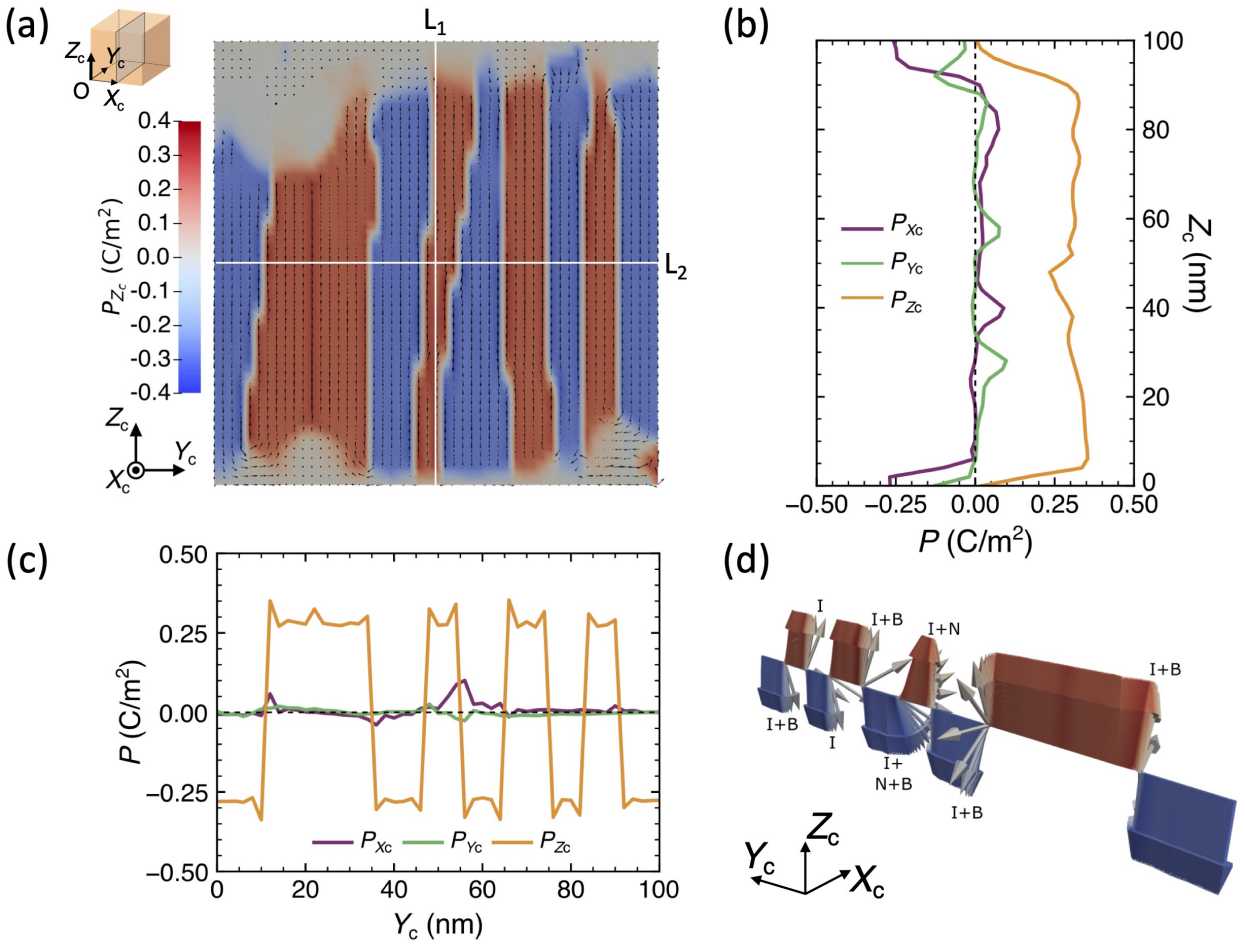

Figure 5: **Polarization components distribution at equilibrium in the middle plane $X_c = 50$ nm of a 100 nm sized cube of BTO**. (a) Planar distribution of the P_{Z_c} component defining the main (OZ_c) polar axis ([001] direction). The alternation of red and blue shadings associated with positive and negative P_{Z_c} components, respectively, illustrates the multiple 180° domains. The black arrow glyphs map the polarization field 3D orientation every 2 nm. Note the small thickness of the surface domains (top and bottom surfaces) with $P^{eq}_{Z_c} \approx 0$. (b) Profiles of the polarization components along the line L_1 ($X_c = 50$ nm, $Y_c = 50$ nm, Z_c) showing the presence of surface domains with polarization perpendicular to the main (OZ_c) polar axis. (c) Profiles of the polarization components along the line L_2 ($X_c = 50$ nm, Y_c, $Z_c = 50$ nm) showing the partial Bloch and Néel nature of some domain walls. (d) 3-dimensional representation of the polarization vector along the same line as in (c), with labeled types of domain walls (B stands for Bloch, N for Néel and I for Ising; I+B, I+N and I+B+N indicate a mixed Ising-Bloch, mixed Ising-Néel and mixed Ising-Bloch-Néel character respectively).

up and down along (OZ_c) like in the bulk (see Figure S13a) and the domain walls are also of Ising type with partial Néel characteristics (Figure S13b).

Let us now focus our attention on the facets of the NC perpendicular to the polar axis, $Z_c = 0$ and $Z_c = 100$ nm. Interestingly, the P_{Z_c} component of the polarization field vanishes near the surface of these facets (see Figure 5a,b). Instead, the polarization lies in the plane of these facets, as shown in Figure 6a and Figure S13c (facet $Z_c = 100$ nm), with mostly tetragonal domains polarized along the (OX_c) direction (representing about 16% of the total NC volume), as well as a lower number of domains polarized along the (OY_c) direction (about 7% of the NC volume). These surface domains extend at an average depth of 8 nm (see Figure 5a,b) from the surface of the $Z_c = 0$ and $Z_c = 100$ nm facets, and they also display Ising domain walls with Bloch and/or Néel characteristics (Figure S13d) like in the core of the nanocrystal (Figure 5d).

Rotation of the polarization from (OZ_c) direction to either (OX_c) or (OY_c) one allows the system to prevent a strong electrostatic depolarizing field. Indeed, the averaged planar electrostatic energy density in the equilibrium structure is mostly zero (see Figure S14). Depolarizing fields, which appear when polarization-induced bound charges are imperfectly screened at an interface, are well known in ferroelectric thin films.[53,54] They are responsible for the emergence of flux closure patterns[49,55] in which the polarization field rotates from the out-of-plane direction to lie in the plane of the thin film surface, similarly to our NCs, as well as for the appearance of more exotic polar textures such as polar vortices,[56] which we do not observe here. Rotation of polarization on surfaces normal to (OZ_c) thus allows the NC to sustain uniformly polarized domains, at the cost of an increase in electromechanical energy near the surfaces. Nonetheless, this is counteracted by the release of elastic energy by the 90° domain walls near the surface (see Figure S14).

Lateral piezoresponse force response simulation. Starting from the equilibrium solution described in the previous paragraph, we now apply a finite electric field to simulate PFM experimental conditions. The BTO nanocrystal is then relaxed under this applied electric field, leading to new equilibrium values of the polarization and mechanical displacement

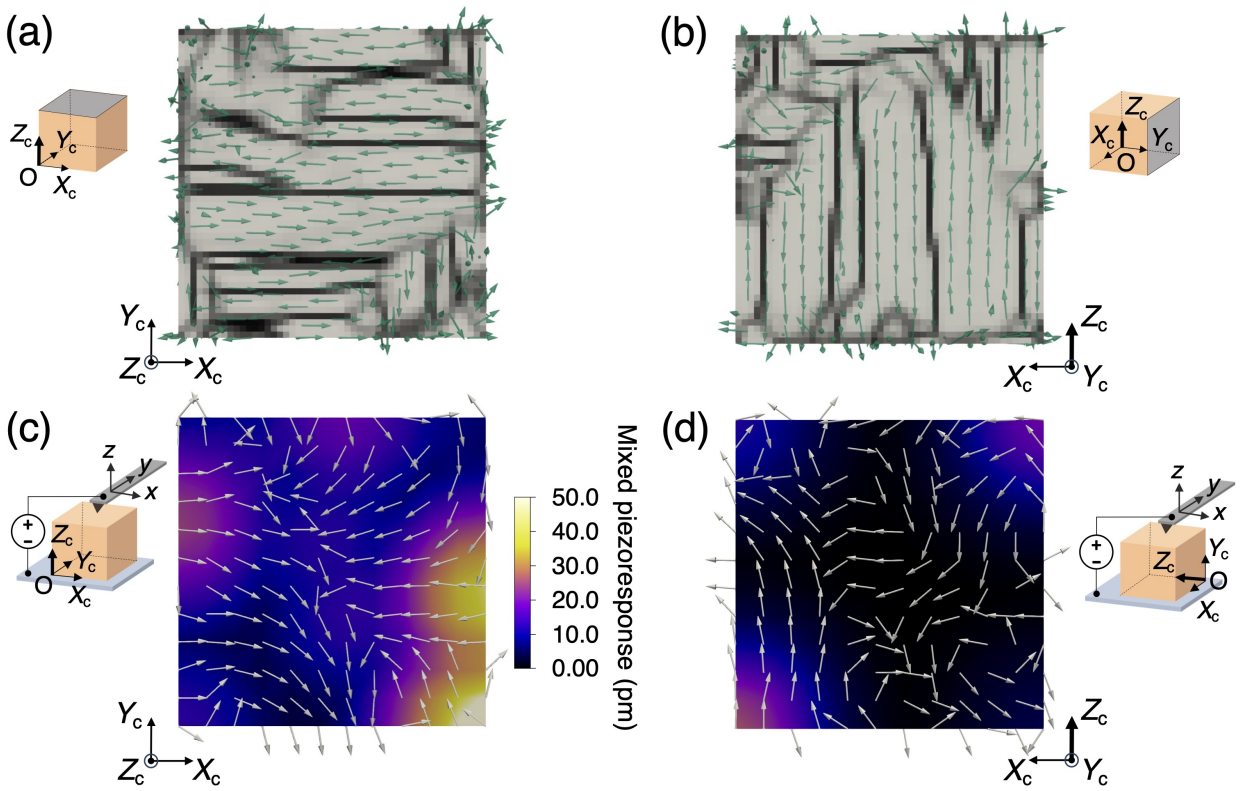

Figure 6: Simulated in-plane polarization texture and piezoresponce of 100 nm sized BTO cube, with polar axis along (OZ_c). (a) Polarization gradient in the $Z_c = 100$ nm (001) plane at equilibrium (at the temperature of 293 K), with light gray indicating domains and dark grey/black indicating domain walls. The solid arrow glyphs (green) represent the orientation of the polarization vector. (b) Polarization gradient in the $Y_c = 100$ nm (010) plane. (c) In-plane mixed piezoresponse in the $Z_c = 100$ nm plane, for a crystal oriented with the Z_c axis parallel to the laboratory z axis, in response to a field of amplitude $E_z = 150$ kV/cm. The solid arrow glyphs indicate the piezoresponse vector orientation at the surface. The color map corresponds to a gaussian resampling of the simulation values of the piezoresponse displacement to better match experiments (kernel standard deviation of ≈ 20 nm, corresponding to the experimental imaging resolution). The largest calculated displacement, located at the bottom-right corner ($Y_c = 0$ nm and $X_c = 100$ nm) is 75 pm, and the displacement in the center of the cube is 4 pm. (d) In-plane mixed piezoresponse in the $Y_c = 100$ nm plane, for a crystal oriented with Z_c axis parallel to laboratory x axis, in response to a field applied along z axis (amplitude $E_z = 150$ kV/cm, very close to the field amplitude applied in the PFM measurements).

fields.

Let us first consider the case when an electric field of amplitude $E_z^{\mathrm{sim}} = 150$ kV/cm is applied along the polar axis (OZ_c) direction of the BTO nanocrystal. The difference between the zero-field and finite-field mechanical displacement fields gives us an estimate

of the electromechanical response of the nanocube. We show, in Figure 6c, the resulting electric-field-induced mixed piezoresponse in the "top" facet perpendicular to the polar axis ($Z_c = 100$ nm facet). We observe qualitatively similar LPFM data of Figure 3i, Figure S10f, S11f and S12f, with local regions of pronounced in-plane displacement at the corners and edges of the facet. We also observe a low to vanishing in-plane piezoelectric displacement in the inner region of the facet, as evidenced experimentally as well.

To investigate the other experimental configuration of the nanocube having its polar axis (OZ_c) lying in the substrate plane, parallel to the laboratory plane (xy), we also simulated the application of an electric field along the (OY_c) axis using the same equilibrium condition as depicted in Figure 5. The resulting mixed piezoresponse simulation, presented on Figure 6d, exhibits lower (by one order of magnitude in the center of the facet and by a factor of 2 to 5 at the edges) and contrast than the simulation for the field applied along (OZ_c). It is well known that the presence of 90° twin domain walls contribute to the piezoelectric response of BTO[57–59] and can strongly enhance it. Indeed, contrary to the (OY_c) facet, the (OZ_c) possesses multiple 90° domain walls, at a distance of about 8 nm from the surface, due to a 90° rotation of the polarization from a Z_c axis aligned orientation (as displayed for $X_c = 0$ nm facet in Figure S13a) to an in-(X_c, Y_c) plane lying one. This may explain the larger simulated in-plane electromechanical response when the electric field is applied along the Z_c axis (Figure 6c).

We note that the magnitude of the maximum in-plane displacement observed experimentally (Figure 3i) is one order of magnitude larger than that obtained from the simulation (Figure 6b). Apart from the fact that we did not calibrate PFM lateral displacement, two other factors may contribute to this difference. First, in the experiment the amplitude of the electric field effectively applied to the nanocrystal is not known precisely because the PFM geometry results in a pronounced inhomogeneous radial distribution with a larger field valued compared to the one of the uniform field applied in the simulations (considering the same applied voltage). Second, in the simulations the applied electric field is static, while the

PFM tip applies an AC voltage oscillating at a frequency set close to the electromechanical resonance, hence enhancing the displacement.

Conclusion

It is now well established theoretically and experimentally, that ferroelectric materials at the nanoscale exhibit exotic polarization texture, leading to unconventional properties. The case of 0-dimension ferroelectric nanocrystals, in particular isolated ones, has been far less studied experimentally, despite the opportunity it offers to bring novel properties due to their large surface to volume ratio. In this work we considered isolated barium titanate nanocrystals immobilized on a conductive surface and exposed to air. Using a solvothermal approach[19] we were able to synthesize NC of a well-defined cubic shape and 160 nm average size, that conserve the tetragonal structure of BTO at room temperature (293 K), are individual monocrystallites (as observed by TEM) and exhibit the expected transition to a cubic symmetry phase above 120°C, the known Curie temperature of the ferro- to para-electric phases. We then investigated, at room temperature, the inverse piezoelectric properties of such pristine individual NC by piezoresponse force microscopy. To this end, we developed a methodology that combines the firm attachment of the NC to the substrate with a conductive polymer and the fine adjustment of the deflection laser in a position along the PFM cantilever that strongly reduces electrostatic artifacts.[47] This strategy allowed repeated measurements on the same particle without risk of being dragged with the PFM tip and provided a high confidence in the crystal deformation fields recorded. We observed that none of the NC showed any vertical PFM displacement, while all showed lateral displacements. We reconstructed mixed piezoresponse fields from the 2D LPFM recording of the same NC for two orthogonal orientations relative to the cantilever (attached to the laboratory frame). All the NC studied showed an inhomogeneous LPFM field of larger amplitude along the edges, a minimum at the center with deformations that tend to be oriented towards this

lower-amplitude central region.

To check whether these observations were consistent with the underlying texture of the volume polarization, we conducted phase field simulations.[15,17] These simulations revealed that in the equilibrium state at the temperature of 293 K, a polar axis (OZ_c) with up and down 180° domains emerges in the core, accompanied with 90° domains on the two surfaces normal to this axis in a layer of an average thickness of 8 nm. In this layer, there is a dominant polarization orientation in the plane with mostly 180° and a few 90° domains (on the edges). Hence, the phase field simulations predict that none of the cube facets possess an out-of-plane polarization component, which is consistent with the PFM observations. We investigated the nature of the domain walls, as predicted by the simulation, and found that they are mostly of the Ising type with Bloch and/or Néel characteristics. We then simulated the LPFM field by calculating the difference between the equilibrium position of atomic displacement in the zero electric field and in the presence of an amplitude-similar electric field as applied during the PFM measurement. The resulting simulated LPFM 2D-maps strongly resemble the experimental ones, with maximum displacement amplitudes along the edges and in the corners, and displacement vectors mostly following the gradient of amplitude.

The results of our study challenge the interpretation of second harmonic generation (SHG) by ≈ 100 nm-sized BTO nanocrystals, implicitly considered composed of a single static polarization domain in all reported studies,[60] eventually bearing a cubic symmetry shell.[61] As the 180° domains dominate the core and surface of the NC in a balanced up- and down-fraction, we expect that it yields a destructively interfering SHG field, leaving open the origin of the observed nonlinear contrast. Correlative SHG and PFM investigations may contribute to resolve this issue. Finally, ferroelectric matrices doped with luminescent reporting ionic species have also been considered for sensing applications, including temperature[62] and electric fields.[63,64] The complex polarization structure of BTO nanocrystals that we revealed in our study should be considered to design optimal ferroelectric-based nanosensors.

Materials and Methods

Sample preparation

BTO nanocube synthesis and characterization. Barium titanate nanocrystals were synthesized using the solvothermal method described in Bogicevic *et al.*[19] Briefly, in a solvent made of volumic proportions of 60% ethanol and 40% deionized water, we mixed, in a nitrogen environment, solid $Na_2Ti_3O_7$ titanium and soluble $Ba(OH)_2 \cdot 8H_2O$ barium precursors. We then heated the mixture at 250°C in an autoclave under autogeneous pressure for 24 hours. We selected a Ba/Ti atomic ratio of 1.6 as it leads to BTO nanocrystals of mostly cubic shape and relatively homogeneous size, as can be observed on Figure S1a SEM image, in the range of 100-350 nm.

XRD measurement (Figure 1b) was performed at 293 K using the Cu Kα1 (λ= 1.5418 Å) and Cu Kα2 radiations (λ= 1.5444 Å) of a diffractometer (D2 Phaser from Bruker AXS GmbH, Germany) and collecting data in steps of 0.02°. We then extracted the structural model with DIFFRAC.EVA (Bruker) software, and performed Rietveld refinement of the structural model using the WinPlotr/FullProf package[65] with peak shape described by a pseudo-Voigt function and background level modelled using a polynomial function. The refined free parameters were background coefficients, scale factor, lattice constants, zero shift, peak profile, and asymmetry parameters.

For single BTO NC experiments, we prepared an aqueous colloidal suspension of BTO NC at the stock concentration of 1 mg/mL.

BTO NC immobilization. To enable contact mode PFM imaging on individual BTO NC, we immobilize them on a 170 μm thick glass coverslip with a conductive 80 nm-thick layer of indium-tin-oxide (ITO) deposited on it. Furthermore, a numbered grid made by gold-deposition and with the smallest cells of 30 μm size was deposited on the ITO-coated coverslip. This allows us to address the same individual BTO NC after 90° rotation and also

with other analytical methods. For immobilization while maintaining electrical contact, we first spin-coated a 40-80 nm thick layer of an aqueous suspension (at 1% weight concentration) of a conductive polymer PEDOT:PSS (Ref. 768618, Sigma Aldrich) onto the marked ITO-coated coverslip. Subsequently, the stock solution of BTO NCs was first diluted by a factor of 50 in water, then spin-coated onto the coated coverslip and the sample was finally annealed at 95°C for 30 minutes. While the literature suggests annealing PEDOT:PSS at temperatures ranging from 80°C to 160°C, we deliberately maintained the annealing temperature below 100°C to avoid any potential phase transition of BTO, which typically occurs at a Curie temperature of 120°C.

PFM measurements

For PFM we used a commercial apparatus (Dimension ICON head system and Nanoscope V controller, Bruker Inc.). The measurements were conducted using SCM-PIT-V2 (Bruker) probes, which have conductive platinum-iridium coated tips with a radius of curvature of 25 nm and a nominal spring constant of 3 N/m. We acquired the piezoresponse phase and amplitude signal while scanning the tip along the laboratory frame x axis direction (see Figure 2b), with the cantilever along y axis.

Minimization of electrostatic effects. It is widely recognized that PFM measurements can exhibit artifacts, leading to possible misinterpretations of the data. The signal artifacts are mainly caused by non-electromechanical effects such as electrostatic force that arises due to the electrostatic potential difference between the cantilever and the sample.[66] This force generates a bending response in the cantilever of the AFM that is not distinguishable from the true PFM signal. The strength of this force is highest near the tip-sample junction and decreases with increasing distance along the cantilever. To address this issue, we employed the concept of electrostatic blind spot position (ESBS) for the laser, as recently introduced by Killgore *et al.*[47] In ESBS, the laser spot, which is usually placed just above the tip,

is positioned along the cantilever where the bending induced by the electrostatic force is minimised, in order to get a piezoresponse amplitude dominated by the electromecanichal contribution. The signal thus obtained will be predominantly dominated by the true PFM signal caused by the bending of the cantilever due to inverse piezoelectric effect. The ESBS position was determined to be at a distance of 0.45 times the length of the cantilever.

PFM measurements were done on single isolated BTO NCs preidentified using scanning electron microscopy (SEM). The lateral PFM phase and amplitude images were taken using a drive voltage of 1.5 V and a drive frequency of 727.856 kHz (near in-plane contact resonance of the cantilever). We used a scan speed of 0.35 Hz and utilized 192 scan lines across a full scan size of 300 nm resulting in 1.56 nm pixel size.

LPFM phase offset φ_{offset} estimation. To estimate φ_{offset}, we first selected one domain with the smallest phase values, close to 0, as the reference, and computed a first phase offset as the phase average value within this domain. In parallel, we identified another domain with phase values close to 180°. Subtracting 180° from the phase of this second domain led to a second phase offset. By averaging these offsets, we obtained a final offset value of $-12 \pm 2°$ for the PFM scan along the $(\mathrm{O}X_{\mathrm{c}})$ direction. The same process was repeated for the PFM scan along the $(\mathrm{O}Y_{\mathrm{c}})$ direction, producing an average offset value of $-9 \pm 4°$. As this offset is attributed to the instrumental response and should be the same for both scans, regardless of particle orientation, we took the average of these two values, resulting in $\varphi_{\text{offset}} = -10 \pm 2°$.

Vector lateral PFM mapping. To build the $\boldsymbol{u}^{\mathrm{m}}$ lateral displacement field of probed-NC facets, we first had to register $u_{Y_{\mathrm{c}}}$ component map with $u_{X_{\mathrm{c}}}$ map, as they were acquired separately. We only considered translations shifts between the two scans, as rotation mismatch could not be assessed with a precision better than the uncertainty on the physical 90° sample rotation. The translation vector shift between X_{c} and Y_{c} components was determined using Fiji-ImageJ software,[67] based on the largest overlap of the raw PFM amplitude images. We then represented the mixed displacement amplitude and vector map.

Piezoresponse simulation

Simulations of an embedded BTO nanoparticle have been performed using FERRET,[15] a module for simulating multiferroic phenomena in the MOOSE finite element framework.[48] We consider the equilibrium domain structure and piezoresponse of a stress-free BTO nanocube (100 nm size) embedded in a dielectric infinite medium (here assumed to be air), by evolving a time-dependent Landau-Ginzburg-Devonshire equation, $\frac{\delta \boldsymbol{P}}{\delta t} = -\frac{\delta F}{\delta \boldsymbol{P}}$, with F representing the free energy of the system.

The Helmoltz free energy volume density f includes several terms, introduced in Hlinka and Marton[51] and which analytical expressions are given in the Supporting Information Text S2:

$$f_{\mathrm{H}} \equiv f_{\mathrm{bulk}} + f_{\nabla P} + f_{\mathrm{elastic}} + f_{\mathrm{electrostr}} + f_{\mathrm{elec}}, \tag{1}$$

where f_{bulk} is the contribution to the energy stemming from the local polarization field $\boldsymbol{P}(\boldsymbol{r})$. In a uniaxial ferroelectric, this typically has two degenerate minima and a double-well shape as a function of the polarization value. This is typically the case in BTO and indicates the desire of the system to form a uniformly polarized ferroelectric domain. The term $f_{\nabla P}$ depends on the gradient of the polarization field and tends to oppose variations of the polarization field. The term f_{elastic} depends on the derivative of the local atomic displacement field $\boldsymbol{u}(\boldsymbol{r})$ (defined relative to a cubic parent lattice structure) and describes the linear elastic response of the system. The electrostrictive term $f_{\mathrm{electrostr}}$ gathers the electromechanical energy couplings between the polarization field $\boldsymbol{P}(\boldsymbol{r})$ and the displacement field $\boldsymbol{u}(\boldsymbol{r})$. Finally, f_{elec} represents the energy density caused by internal/external electric fields. As stated earlier, as we consider a stress-free condition, the strain energy term $-\boldsymbol{\sigma}.\boldsymbol{\varepsilon}$, where $\boldsymbol{\sigma}$ is the stress and $\boldsymbol{\varepsilon}$ the strain tensor, resumes at zero. To realize our simulations of ferroelectric domains and displacements on the BTO NC at the ambient temperature of 298 K, we adopted numerical coefficients from ref.[51] for the numerical values of the coefficients involved in each term of energy density. The displacement field is obtained by solving the stress-divergence equation

$\nabla.\boldsymbol{\sigma} = 0$ (neglecting gravity) with mechanical boundary conditions without stress at each time step.

The computational domain comprises the BTO nanocrystal, with 100 nm long sides embedded at the center of a dielectric matrix, with 200 nm sides in order to capture the depolarization field around the inclusion. The relative permittivity of the dielectric matrix is set to 1 and the NC is considered stress-free, simulating an open air environment. Dirichlet boundary conditions on (u, Φ), are applied to ensure that displacement and electrostatic fields disappear far from the particle. Partial clamping and dielectric screening by PEDOT:PSS could lead to a slight alteration of the ground state and the piezoelectric response through modulation of the surface layer thickness and potential Poisson effects which could lead to enhanced out-of-plane mechanical response.

The equilibrium structure at zero applied electric field is obtained by relaxing the system starting from a reasonable approximation of the paraelectric state, realized by initializing random, small component ($< 10^{-4}\mathrm{C/m^2}$) values to the polarization and local displacement fields. Through the gradient flow approach, the system variables are evolved through a dynamic time stepper until a local minimum is reached, defined by a convergence criterion of within $10^{-6}\%$ of the total energy of the previous time step.

The average thickness of the surface layers are estimated by the ratio of the volume having $P_{Z_c} \approx 0$ to the volume of the nanocrystal, multiplied by the nanoparticle size. The obtained averaged thickness of 8 nm correlates well with typical thicknesses which can be estimated from Figure 5b.

Coupling to internal/external electrical fields is accomplished through the Poisson equation, $\nabla^2\Phi = \frac{1}{\varepsilon_r\varepsilon_0}\nabla.\boldsymbol{P}$, where Φ is the electric potential, related to the electric field $\boldsymbol{E}$ through $\boldsymbol{E} = -\nabla\Phi$, and ε_r is the surrounding medium relative permittivity, which in our case is air for most of the particle volume, hence $\varepsilon_r = 1$. Hence, to mimic PFM experiments, we use the following procedure. First, we start with the zero-field equilibrium structure. We then relax the polarization and local displacement fields by solving the Landau-Ginzburg-

Devonshire equation and the stress-divergence equation at each time step, under an applied external electric field of 150 kV/cm, until the new equilibrium is reached. The difference in equilibrium local displacement fields between the configuration with and without applied electric field gives us the electric-field induced displacement in the BTO nanocube, which we report in Figure 6c,d and compare to lateral PFM experiments. Note that to compare with the experimental observations, a Gaussian blur with 20 nm diameter was applied to the local displacement field.

Author contributions

Conceptualization: BD, CFD, CP, and FT; Methodology: AM, KC, KP, CFD, CP and FT; Software: KC and CP; Validation: AM, KC, CFD, CP and FT; Formal analysis: KC and CP; Investigation: AM, AZ, MV, and KC; Resources: CB and FK; Data curation: CB, MV, AM and KC; Writing – Original draft: AM, KC, CP and FT; Writing – Review and Editing: CFD, KP, CP and FT; Visualization: AM, KC, MV, AZ, KP, CP, and FT; Supervision: CFD and FT ; Project administration: CFD, CP and FT; Funding acquisition: BD, CP, CFD and FT. All authors have read and agreed to the published version of the manuscript.

Acknowledgement

We thank Pascale Gemeiner for the measurements of the temperature dependence of the BTO Raman spectrum. The authors thank Nataliya Alyabyeva for her initial support in PFM imaging and Dana Stanescu and Cindy Rountree for their training on the Bruker Icon PFM of the CEA/SPEC Interdisciplinary Multiscale Atomic Force Microscope Platform. The authors thank Pierre Audebert, Guy Deniau, and Noelle Gogneau for their suggestions to bind the nanocrystals to the substrate; Laureen Moreau for her guidance in SEM imaging; and Simon Vassant for the realization of the marking grids enabling correlative SEM-PFM imaging. C.P. and K.C. acknowledge support from GENCI-TGCC computing

resources through grant AD010913519 and computational resources from the "Mésocentre" computing center of Université Paris-Saclay, CentraleSupélec and École Normale Supérieure Paris-Saclay supported by CNRS and Région Île-de-France (https://mesocentre.universite-paris-saclay.fr/). This work has received financial support to B.D., C.F. and F.T. from the CNRS through the MITI interdisciplinary program and from the French National Research Agency (ANR, grant numbers ANR-21-CE09-0028 and ANR-21-CE09-0033).

Supporting Information Available

Two supporting texts: PFM basics; analytical expressions of the contributions to the free energy volume density used in phase field simulations. Supporting data figures: Additional characterizations of the BTO sample (morphology and strain, HR-STEM images, temperature-dependent Raman spectroscopy and Curie temperature determination, PEDOT:PSS layer thickness measurement, size distribution of BTO NC inferred from SEM measurements); Evidence of non-electromechanical effects and use of ESBS setting to suppress them; LPFM resonance curve of a cantilever; Lateral PFM mapping of three additional BTO NC; Additional data on phase field simulations (distribution of polarization in facets orthogonal or parallel to the polar axis, distribution of the different components of the energy density across a NC).

References

1. Mikolajick, T.; Slesazeck, S.; Mulaosmanovic, H.; Park, M. H.; Fichtner, S.; Lomenzo, P. D.; Hoffmann, M.; Schroeder, U. Next generation ferroelectric materials for semiconductor process integration and their applications. *Journal of Applied Physics* **2021**, *129*.

2. Naumov, I. I.; Bellaiche, L.; Fu, H. Unusual phase transitions in ferroelectric nanodisks and nanorods. *Nature* **2004**, *432*, 737–740.

3. Louis, L.; Kornev, I. A.; Geneste, G.; Dkhil, B.; Bellaiche, L. Novel complex phenomena in ferroelectric nanocomposites. *Journal of Physics: Condensed Matter* **2012**, *24*, 402201.

4. Prosandeev, S.; Bellaiche, L. Controlling Double Vortex States in Low-Dimensional Dipolar Systems. *Physical Review Letters* **2008**, *101*, 097203.

5. Nahas, Y.; Prokhorenko, S.; Louis, L.; Gui, Z.; Kornev, I. A.; Bellaiche, L. Discovery of stable skyrmionic state in ferroelectric nanocomposites. *Nature Communications* **2015**, *6*, 8542.

6. Nahas, Y.; Prokhorenko, S.; Kornev, I. A.; Bellaiche, L. Emergent Berezinskii-Kosterlitz-Thouless Phase in Low-Dimensional Ferroelectrics. *Physical Review Letters* **2017**, *119*, 117601.

7. Gonçalves, M. A.; Escorihuela-Sayalero, C.; Garca-Fernández, P.; Junquera, J.; Íñiguez, J. Theoretical guidelines to create and tune electric skyrmion bubbles. *Science Advances* **2019**, *5*, 1–6.

8. Balke, N.; Winchester, B.; Ren, W.; Chu, Y. H.; Morozovska, A. N.; Eliseev, E. a.; Huijben, M.; Vasudevan, R. K.; Maksymovych, P.; Britson, J.; Jesse, S.; Kornev, I. A.; Ramesh, R.; Bellaiche, L.; Chen, L.-Q.; Kalinin, S. V. Enhanced electric conductivity at ferroelectric vortex cores in $BiFeO_3$. *Nature Physics* **2011**, *8*, 81–88.

9. Yadav, A. K.; Nelson, C. T.; Hsu, S. L.; Hong, Z.; Clarkson, J. D.; Schlepütz, C. M.; Damodaran, A. R.; Shafer, P.; Arenholz, E.; Dedon, L. R.; Chen, D.; Vishwanath, A.; Minor, A. M.; Chen, L.-Q.; Scott, J. F.; Martin, L. W.; Ramesh, R. Observation of polar vortices in oxide superlattices. *Nature* **2016**, *530*, 198–201.

10. Das, S.; Tang, Y. L.; Hong, Z.; Gonçalves, M. A. P.; McCarter, M. R.; Klewe, C.; Nguyen, K. X.; Gómez-Ortiz, F.; Shafer, P.; Arenholz, E.; Stoica, V. A.; Hsu, S.-L.; Wang, B.; Ophus, C.; Liu, J. F.; Nelson, C. T.; Saremi, S.; Prasad, B.; Mei, A. B.; Schlom, D. G. *et al.* Observation of room-temperature polar skyrmions. *Nature* **2019**, *568*, 368–372.

11. Abid, A. Y.; Sun, Y.; Hou, X.; Tan, C.; Zhong, X.; Zhu, R.; Chen, H.; Qu, K.; Li, Y.; Wu, M.; Zhang, J.; Wang, J.; Liu, K.; Bai, X.; Yu, D.; Ouyang, X.; Wang, J.; Li, J.; Gao, P. Creating polar antivortex in $PbTiO_3/SrTiO_3$ superlattice. *Nature Communications* **2021**, *12*, 2054.

12. Tan, C.; Dong, Y.; Sun, Y.; Liu, C.; Chen, P.; Zhong, X.; Zhu, R.; Liu, M.; Zhang, J.; Wang, J.; Liu, K.; Bai, X.; Yu, D.; Ouyang, X.; Wang, J.; Gao, P.; Luo, Z.; Li, J. Engineering polar vortex from topologically trivial domain architecture. *Nature Communications* **2021**, *12*, 4620.

13. Das, S.; Hong, Z.; Stoica, V. A.; Gonçalves, M. A. P.; Shao, Y. T.; Parsonnet, E.; Marksz, E. J.; Saremi, S.; McCarter, M. R.; Reynoso, A.; Long, C. J.; Hagerstrom, A. M.; Meyers, D.; Ravi, V.; Prasad, B.; Zhou, H.; Zhang, Z.; Wen, H.; Gómez-Ortiz, F.; García-Fernández, P. *et al.* Local negative permittivity and topological phase transition in polar skyrmions. *Nature Materials* **2021**, *20*, 194–201.

14. Li, Z.; Wang, Y.; Tian, G.; Li, P.; Zhao, L.; Zhang, F.; Yao, J.; Fan, H.; Song, X.; Chen, D.; Fan, Z.; Qin, M.; Zeng, M.; Zhang, Z.; Lu, X.; Hu, S.; Lei, C.; Zhu, Q.; Li, J.; Gao, X. *et al.* High-density array of ferroelectric nanodots with robust and reversibly switchable topological domain states. *Science Advances* **2017**, *3*, 1–9.

15. Mangeri, J.; Espinal, Y.; Jokisaari, A.; Pamir Alpay, S.; Nakhmanson, S.; Heinonen, O. Topological phase transformations and intrinsic size effects in ferroelectric nanoparticles. *Nanoscale* **2017**, *9*, 1616–1624.

16. Luk'yanchuk, I.; Tikhonov, Y.; Razumnaya, A.; Vinokur, V. M. Hopfions emerge in ferroelectrics. *Nature Communications* **2020**, *11*, 2433.

17. Co, K.; Pamir Alpay, S.; Nakhmanson, S.; Mangeri, J. Surface charge mediated polar response in ferroelectric nanoparticles. *Applied Physics Letters* **2021**, *119*.

18. Kwei, G. H.; Lawson, A. C.; Billinge, S. J. L.; Cheong, S. W. Structures of the ferroelectric phases of barium titanate. *The Journal of Physical Chemistry* **1993**, *97*, 2368–2377.

19. Bogicevic, C.; Thorner, G.; Karolak, F.; Haghi-Ashtiani, P.; Kiat, J.-M. Morphogenesis mechanisms in the solvothermal synthesis of $BaTiO_3$ from titanate nanorods and nanotubes. *Nanoscale* **2015**, *7*, 3594–3603.

20. Jiang, B.; Iocozzia, J.; Zhao, L.; Zhang, H.; Harn, Y.-W.; Chen, Y.; Lin, Z. Barium titanate at the nanoscale: controlled synthesis and dielectric and ferroelectric properties. *Chemical Society Reviews* **2019**, *48*, 1194–1228.

21. Smith, M. B.; Page, K.; Siegrist, T.; Redmond, P. L.; Walter, E. C.; Seshadri, R.; Brus, L. E.; Steigerwald, M. L. Crystal Structure and the Paraelectric-to-Ferroelectric Phase Transition of Nanoscale $BaTiO_3$. *Journal of the American Chemical Society* **2008**, *130*, 6955–6963.

22. Cui, Y.; Briscoe, J.; Dunn, S. Effect of Ferroelectricity on Solar-Light-Driven Photocatalytic Activity of $BaTiO_3$ —Influence on the Carrier Separation and Stern Layer Formation. *Chemistry of Materials* **2013**, *25*, 4215–4223.

23. Paillard, C.; Bai, X.; Infante, I. C.; Guennou, M.; Geneste, G.; Alexe, M.; Kreisel, J.; Dkhil, B. Photovoltaics with Ferroelectrics: Current Status and Beyond. *Advanced Materials* **2016**, *28*, 5153–5168.

24. Li, Y.; Li, J.; Yang, W.; Wang, X. Implementation of ferroelectric materials in photocatalytic and photoelectrochemical water splitting. *Nanoscale Horizons* **2020**, *5*, 1174–1187.

25. Hao, Y.; Feng, Z.; Banerjee, S.; Wang, X.; Billinge, S. J.; Wang, J.; Jin, K.; Bi, K.; Li, L. Ferroelectric state and polarization switching behaviour of ultrafine $BaTiO_3$ nanoparticles with large-scale size uniformity. *Journal of Materials Chemistry C* **2021**, *9*, 5267–5276.

26. Abbasi, P.; Barone, M. R.; de la Paz Cruz-Jáuregui, M.; Valdespino-Padilla, D.; Paik, H.; Kim, T.; Kornblum, L.; Schlom, D. G.; Pascal, T. A.; Fenning, D. P. Ferroelectric Modulation of Surface Electronic States in $BaTiO_3$ for Enhanced Hydrogen Evolution Activity. *Nano Letters* **2022**,

27. Neige, E.; Schwab, T.; Musso, M.; Berger, T.; Bourret, G. R.; Diwald, O. Charge Separation in $BaTiO_3$ Nanocrystals: Spontaneous Polarization Versus Point Defect Chemistry. *Small* **2023**, *19*.

28. Assavachin, S.; Osterloh, F. E. Ferroelectric Polarization in $BaTiO_3$ Nanocrystals Controls Photoelectrochemical Water Oxidation and Photocatalytic Hydrogen Evolution. *Journal of the American Chemical Society* **2023**,

29. Schilling, A.; Byrne, D.; Catalan, G.; Webber, K. G.; Genenko, Y. A.; Wu, G. S.; Scott, J. F.; Gregg, J. M. Domains in Ferroelectric Nanodots. *Nano Letters* **2009**, *9*, 3359–3364.

30. Denneulin, T.; Everhardt, A. S. A transmission electron microscopy study of low-strain epitaxial $BaTiO_3$ grown onto $NdScO_3$. *Journal of Physics: Condensed Matter* **2022**, *34*, 235701.

31. Campanini, M.; Erni, R.; Rossell, M. D. Probing local order in multiferroics by transmission electron microscopy. *Physical Sciences Reviews* **2019**, *5*, 20190068.

32. Polking, M. J.; Han, M.-G.; Yourdkhani, A.; Petkov, V.; Kisielowski, C. F.; Volkov, V. V.; Zhu, Y.; Caruntu, G.; Alivisatos, A. P.; Ramesh, R. Ferroelectric order in individual nanometre-scale crystals. *Nature Materials* **2012**, *11*, 700–709.

33. Karpov, D.; Liu, Z.; Rolo, T. d. S.; Harder, R.; Balachandran, P. V.; Xue, D.; Lookman, T.; Fohtung, E. Three-dimensional imaging of vortex structure in a ferroelectric nanoparticle driven by an electric field. *Nature Communications* **2017**, *8*, 280.

34. Megaw, H. Crystal Structure of Barium Titanate. *Nature* **1945**, *155*, 484–485.

35. Huang, Y.; Lu, B.; Li, D.; Tang, Z.; Yao, Y.; Tao, T.; Liang, B.; Lu, S. Control of tetragonality via dehydroxylation of $BaTiO_3$ ultrafine powders. *Ceramics International* **2017**, *43*, 16462–16466.

36. Lee, H.; Moon, S.; Choi, C.; Kim, D. K. Synthesis and Size Control of Tetragonal Barium Titanate Nanopowders by Facile Solvothermal Method. *Journal of the American Ceramic Society* **2012**, *95*, 2429–2434.

37. Zhu, X.; Zhang, Z.; Zhu, J.; Zhou, S.; Liu, Z. Morphology and atomic-scale surface structure of barium titanate nanocrystals formed at hydrothermal conditions. *Journal of Crystal Growth* **2009**, *311*, 2437–2442.

38. Vivekanandan, R.; Kutty, T. Characterization of barium titanate fine powders formed from hydrothermal crystallization. *Powder Technology* **1989**, *57*, 181–192.

39. Suzana, A. F.; Liu, S.; Diao, J.; Wu, L.; Assefa, T. A.; Abeykoon, M.; Harder, R.; Cha, W.; Bozin, E. S.; Robinson, I. K. Structural Explanation of the Dielectric Enhancement of Barium Titanate Nanoparticles Grown under Hydrothermal Conditions. *Advanced Functional Materials* **2023**, *33*.

40. DiDomenico, M.; Wemple, S. H.; Porto, S. P. S.; Bauman, R. P. Raman Spectrum of Single-Domain $BaTiO_3$. *Physical Review* **1968**, *174*, 522–530.

41. Begg, B. D.; Finnie, K. S.; Vance, E. R. Raman Study of the Relationship between Room-Temperature Tetragonality and the Curie Point of Barium Titanate. *Journal of the American Ceramic Society* **1996**, *79*, 2666–2672.

42. Kalinin, S. V.; Rodriguez, B. J.; Jesse, S.; Shin, J.; Baddorf, A. P.; Gupta, P.; Jain, H.; Williams, D. B.; Gruverman, A. Vector Piezoresponse Force Microscopy. *Microscopy and Microanalysis* **2006**, *12*, 206–220.

43. Zhang, H.-Y.; Chen, X.-G.; Tang, Y.-Y.; Liao, W.-Q.; Di, F.-F.; Mu, X.; Peng, H.; Xiong, R.-G. PFM (piezoresponse force microscopy)-aided design for molecular ferroelectrics. *Chemical Society Reviews* **2021**, *50*, 8248–8278.

44. Gruverman, A.; Alexe, M.; Meier, D. Piezoresponse force microscopy and nanoferroic phenomena. *Nature Communications* **2019**, *10*, 1661.

45. Kalinin, S. V.; Rodriguez, B. J.; Jesse, S.; Karapetian, E.; Mirman, B.; Eliseev, E. A.; Morozovska, A. N. Nanoscale Electromechanics of Ferroelectric and Biological Systems: A New Dimension in Scanning Probe Microscopy. *Annual Review of Materials Research* **2007**, *37*, 189–238.

46. Li, X.; Wang, B.; Zhang, T.-Y.; Su, Y. Water Adsorption and Dissociation on $BaTiO_3$ Single-Crystal Surfaces. *The Journal of Physical Chemistry C* **2014**, *118*, 15910–15918.

47. Killgore, J. P.; Robins, L.; Collins, L. Electrostatically-blind quantitative piezoresponse force microscopy free of distributed-force artifacts. *Nanoscale Advances* **2022**, *4*, 2036–2045.

48. Lindsay, A. D.; Gaston, D. R.; Permann, C. J.; Miller, J. M.; Andrš, D.; Slaughter, A. E.; Kong, F.; Hansel, J.; Carlsen, R. W.; Icenhour, C.; Harbour, L.; Giudicelli, G. L.; Stogner, R. H.; German, P.; Badger, J.; Biswas, S.; Chapuis, L.; Green, C.; Hales, J.; Hu, T. *et al.* 2.0 - MOOSE: Enabling massively parallel multiphysics simulation. *SoftwareX* **2022**, *20*, 101202.

49. Prosandeev, S.; Bellaiche, L. Asymmetric screening of the depolarizing field in a ferroelectric thin film. *Physical Review B* **2007**, *75*, 172109.

50. Wieder, H. H. Electrical Behavior of Barium Titanate Single Crystals at Low Temperatures. *Physical Review* **1955**, *99*, 1161–1165.

51. Hlinka, J.; Marton, P. Phenomenological model of a 90° domain wall in $BaTiO_3$-type ferroelectrics. *Physical Review B* **2006**, *74*, 104104.

52. Wang, J. J.; Meng, F. Y.; Ma, X. Q.; Xu, M. X.; Chen, L. Q. Lattice, elastic, polarization, and electrostrictive properties of $BaTiO_3$ from first-principles. *Journal of Applied Physics* **2010**, *108*.

53. Mehta, R. R.; Silverman, B. D.; Jacobs, J. T. Depolarization fields in thin ferroelectric films. *Journal of Applied Physics* **1973**, *44*, 3379–3385.

54. Kopal, A.; Bahnik, T.; Fousek, J. Domain formation in thin ferroelectric films: The role of depolarization energy. *Ferroelectrics* **1997**, *202*, 267–274.

55. Aguado-Puente, P.; Junquera, J. Ferromagneticlike Closure Domains in Ferroelectric Ultrathin Films: First-Principles Simulations. *Physical Review Letters* **2008**, *100*, 177601.

56. Hong, Z.; Damodaran, A. R.; Xue, F.; Hsu, S.-L.; Britson, J.; Yadav, A. K.; Nelson, C. T.; Wang, J.-J.; Scott, J. F.; Martin, L. W.; Ramesh, R.; Chen, L.-Q. Stability of Polar Vortex Lattice in Ferroelectric Superlattices. *Nano Letters* **2017**, *17*, 2246–2252.

57. Wada, S.; Yako, K.; Yokoo, K.; Kakemoto, H.; Tsurumi, T. Domain Wall Engineering in Barium Titanate Single Crystals for Enhanced Piezoelectric Properties. *Ferroelectrics* **2006**, *334*, 17–27.

58. Hlinka, J.; Ondrejkovic, P.; Marton, P. The piezoelectric response of nanotwinned $BaTiO_3$. *Nanotechnology* **2009**, *20*, 105709.

59. Ghosh, D.; Sakata, A.; Carter, J.; Thomas, P. A.; Han, H.; Nino, J. C.; Jones, J. L. Domain Wall Displacement is the Origin of Superior Permittivity and Piezoelectricity in $BaTiO_3$ at Intermediate Grain Sizes. *Advanced Functional Materials* **2014**, *24*, 885–896.

60. Karvounis, A.; Timpu, F.; Vogler-Neuling, V. V.; Savo, R.; Grange, R. Barium Titanate Nanostructures and Thin Films for Photonics. *Advanced Optical Materials* **2020**, *8*, 2001249.

61. Rendón-Barraza, C.; Timpu, F.; Grange, R.; Brasselet, S. Crystalline heterogeneity in single ferroelectric nanocrystals revealed by polarized nonlinear microscopy. *Scientific Reports* **2019**, *9*, 1670.

62. Mahata, M. K.; Koppe, T.; Kumar, K.; Hofsäss, H.; Vetter, U. Upconversion photoluminescence of Ho^{3+}-Yb^{3+} doped barium titanate nanocrystallites: Optical tools for structural phase detection and temperature probing. *Scientific Reports* **2020**, *10*, 8775.

63. Hao, J.; Zhang, Y.; Wei, X. Electric-Induced Enhancement and Modulation of Upconversion Photoluminescence in Epitaxial $BaTiO_3$:Yb/Er Thin Films. *Angewandte Chemie International Edition* **2011**, *50*, 6876–6880.

64. Sun, Q.; Wang, W.; Pan, Y.; Liu, Z.; Chen, X.; Ye, M. Effects of temperature and electric field on upconversion luminescence in Er^{3+}-Yb^{3+} codoped $Ba_{0.8}Sr_{0.2}TiO_3$ ferroelectric ceramics. *Journal of the American Ceramic Society* **2017**, *100*, 4661–4669.

65. Rodríguez-Carvajal, J. Recent advances in magnetic structure determination by neutron powder diffraction. *Physica B: Condensed Matter* **1993**, *192*, 55–69.

66. Balke, N.; Maksymovych, P.; Jesse, S.; Herklotz, A.; Tselev, A.; Eom, C.-B.; Kravchenko, I. I.; Yu, P.; Kalinin, S. V. Differentiating Ferroelectric and Nonferroelectric Electromechanical Effects with Scanning Probe Microscopy. *ACS Nano* **2015**, *9*, 6484–6492.

67. Schindelin, J.; Arganda-Carreras, I.; Frise, E.; Kaynig, V.; Longair, M.; Pietzsch, T.; Preibisch, S.; Rueden, C.; Saalfeld, S.; Schmid, B.; Tinevez, J.-Y.; White, D. J.; Hartenstein, V.; Eliceiri, K.; Tomancak, P.; Cardona, A. Fiji: an open-source platform for biological-image analysis. *Nature Methods* **2012**, *9*, 676–682.

Supporting information for: Ferroelectric texture of individual barium titanate nanocrystals

A. Muraleedharan, K. Co, M. Vallet, A. Zaki, F. Karolak, C. Bogicevic, K. Perronet, B. Dkhil, C. Paillard, C. Fiorini, and F. Treussart

1. Supporting text

S1. Basic principles of piezoresponse force microscopy

In piezoresponse force microscopy, a conducting tip to which an oscillating voltage $V_{\mathrm{tip}} = V_{\mathrm{AC}} \cos(2\pi f_{\mathrm{d}} t)$ is applied is brought into contact with the grounded sample, causing a surface deformation due to the inverse piezoelectric effect. From the resulting oscillatory response of the material, the device extracts the first harmonic component of the deflection of the AFM tip $D = A\cos(2\pi f_{\mathrm{d}} t + \varphi)$, where A is the deflection amplitude to which the magnitude of the local piezoresponse displacement u is proportional, and φ is the phase change between the driving voltage and the voltage-induced deformation that depends on the local polarization of the material.[45] The deflection is measured using a laser beam that is reflected off the cantilever onto a position-sensitive quadrant photodiode. PFM cantilever undergoes two types of deformations: vertical deformation due to the out-of-plane/vertical domains (VPFM) or/and torsion due to the shear deformation induced by the in-plane/lateral domains (LPFM). PFM measurement consists of mapping the piezoresponse amplitude and phase signals in both the VPFM and LPFM modes. The electromechanical response of a ferroelectric material of arbitrary crystallographic orientation to an applied voltage is a vector having three independent components of piezoresponse: one VPFM measurement and two LPFM measurements in two independent directions. The third component of the displacement vector can be determined by imaging the sample region of the sample after a 90° rotation around the z axis. When all three components of the piezoresponse are acquired,

it is possible to reconstruct a 3-dimensional local electromechanical mixed response vector map. This approach is called a vector PFM, described in details in Kalinin *et al.*[42]

S2. Phase field simulations: analytical expressions of the contributions to the free energy volume density

In this section, (x, y, z)-coordinates are attached to the material. Unless otherwise specified we use in an indiscriminate manner the letter (x, y, z) or number (1,2,3) indices. Below are the analytical expressions of the different terms of Helmoltz free energy density $f_{\mathrm{H}} \equiv f_{\mathrm{bulk}} + f_{\nabla P} + f_{\mathrm{elastic}} + f_{\mathrm{electrostr}} + f_{\mathrm{elec}}$, as stated in refs.[15,51]

$$\begin{aligned} f_{\mathrm{bulk}} &= \alpha_1(P_x^2 + P_y^2 + P_z^2) + \alpha_{11}^{(e)}(P_x^4 + P_y^4 + P_z^4) \\ &+ \alpha_{12}^{(e)}(P_x^2P_y^2 + P_x^2P_z^2 + P_y^2P_z^2) + \alpha_{111}(P_x^6 + P_y^6 + P_z^6) \\ &+ \alpha_{112}(P_x^4(P_y^2 + P_z^2) + P_y^4(P_x^2 + P_z^2) + P_z^4(P_y^2 + P_x^2)) \\ &+ \alpha_{123}P_x^2P_y^2P_z^2 \end{aligned} \tag{2}$$

The gradient energy density, $f_{\nabla P}$, contains the first-order Lifshitz invariant

$$\begin{aligned} f_{\nabla P} &= \frac{G_{11}}{2}\left(\frac{\partial P_x}{\partial x} + \frac{\partial P_y}{\partial y} + \frac{\partial P_z}{\partial z}\right) \\ &+ G_{14}\left(\frac{\partial P_x}{\partial x}\frac{\partial P_y}{\partial y} + \frac{\partial P_x}{\partial x}\frac{\partial P_z}{\partial z} + \frac{\partial P_z}{\partial z}\frac{\partial P_y}{\partial y}\right) \\ &+ \frac{G_{44}}{2}\left(\left(\frac{\partial P_x}{\partial y}\right)^2 + \left(\frac{\partial P_y}{\partial x}\right)^2 + \left(\frac{\partial P_x}{\partial z}\right)^2 + \left(\frac{\partial P_z}{\partial x}\right)^2 + \left(\frac{\partial P_z}{\partial y}\right)^2 + \left(\frac{\partial P_y}{\partial z}\right)^2\right) \end{aligned} \tag{3}$$

Contributions to the elastic volume energy density comes from the strain tensor $\varepsilon_{\alpha\beta}$ defined in terms of the local displacement field $\boldsymbol{u}(\boldsymbol{r})$:

$$\varepsilon_{\alpha\beta} = \frac{1}{2}\left(\frac{\partial u_\alpha}{\partial \beta} + \frac{\partial u_\beta}{\partial \alpha}\right), \alpha, \beta = x, y \text{ or } z. \tag{4}$$

The elastic energy density is then written in terms of the elastic constants C_{ij}, and using Voigt's notation ($\varepsilon_1 = \varepsilon_{11}, \varepsilon_2 = \varepsilon_{22}, \varepsilon_3 = \varepsilon_{33}, \varepsilon_4 = 2\varepsilon_{23}, \varepsilon_5 = 2\varepsilon_{13}$, and $\varepsilon_6 = 2\varepsilon_{12}$) as

$$\begin{aligned} f_{\text{elastic}} &= \frac{1}{2}C_{11}\left(\varepsilon_1^2 + \varepsilon_2^2 + \varepsilon_3^2\right) \\ &+ C_{12}\left(\varepsilon_1\varepsilon_2 + \varepsilon_1\varepsilon_3 + \varepsilon_2\varepsilon_3\right) \\ &+ \frac{1}{2}C_{44}\left(\varepsilon_4^2 + \varepsilon_5^2 + \varepsilon_6^2\right) \end{aligned} \tag{5}$$

The electrostrain energy density is written

$$\begin{aligned} f_{\text{electrostr}} &= -q_{11}\left[\varepsilon_1 P_x^2 + \varepsilon_2 P_y^2 + \varepsilon_3 P_z^2\right] \\ &- q_{12}\left[\varepsilon_1\left(P_y^2 + P_z^2\right) + \varepsilon_2\left(P_x^2 + P_z^2\right) + \varepsilon_3\left(P_y^2 + P_x^2\right)\right] \\ &- q_{44}\left[\varepsilon_6 P_x P_y + \varepsilon_5 P_x P_z + \varepsilon_4 P_y P_z\right] \end{aligned} \tag{6}$$

At last, the electric energy $f_{\text{elec}} = -\boldsymbol{E}(\boldsymbol{r}).\boldsymbol{P}(\boldsymbol{r})$, where $\boldsymbol{E}(r)$ is the electric field obtained from solving the Poisson equation.

All numerical coefficients involved here were taken from Ref.[51]

2. Supporting data

2.1. BTO sample additional characterizations

BTO nanocrystals morphology and strain

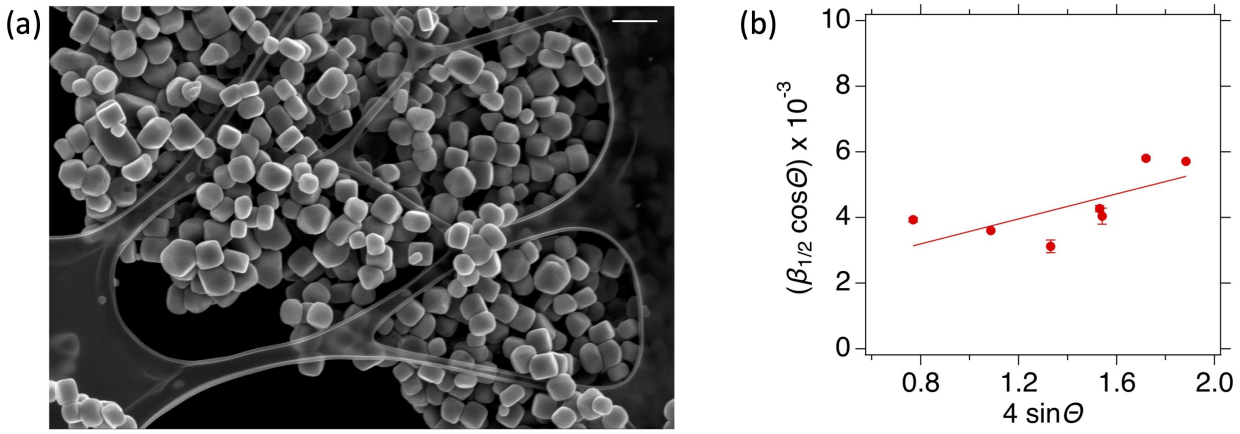

Figure S1: **Morphology and strain of as-produced BTO nanocrystals**. (a) SEM image of BTO NC powder deposited on a carbon layer, showing mostly parallelepipedic/cubic shape particles. SEM model: XL30S FEG from FEI/Philips (The Netherlands). Scale bar: 400 nm. (b) Estimate of the strain from the diffractogram Figure 1a, using Williamson-Hall method. The experimental points are the diffraction peaks positions, and the solid line a fit according to equation (7).

Figure S1a shows a "large" SEM field of view of the as-produced BTO nanocrystal powder. This powder was the starting material to prepare the BTO NC aqueous suspension from which individual particles were isolated. We also estimate the strain from Figure 1a diffractogram of this powder using the Williamson-Hall equation for a Cauchy peak shape:

$$\beta_{1/2}\cos\theta = \frac{K\lambda}{D} + 4e\sin\theta, \tag{7}$$

where $\beta_{1/2}$ is the full-width at half-maximum of each diffraction peak, λ is the X-ray radiation wavelength (here $\lambda = 1.5418$ Å, D and e the grain size and inhomogeneous strain, respectively, and K is a NC form factor that we took equal to 1. Figure S1b displays the experimental points for each diffraction peak and the linear fit according to equation 7, leading

to a strain $e = 0.19 \pm 0.04\%$ and a crystallographic grain size $D = 81$ nm.

HR-STEM Image

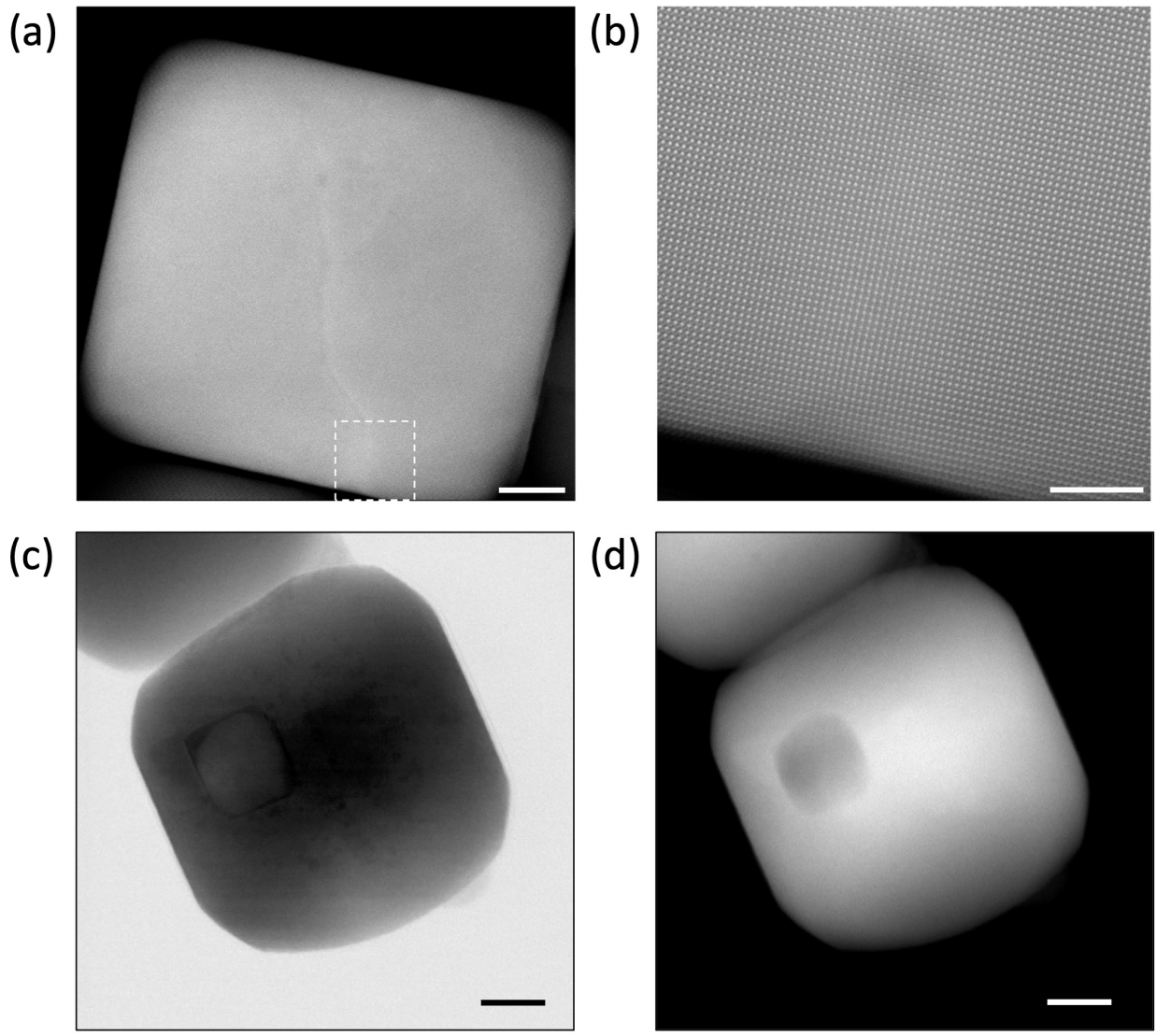

Figure S 2: **Additional STEM images of single BTO nanocrystals**. (a) HAADF STEM image of one BTO NC. Scale bar: 20 nm. (b) Atomic resolution image of the region delineated by the dashed line square in (a), with no evidence of a thin cubic layer at the NC surface. Scale bar: 5 nm. (c) Bright-field and (d) HAADF images of a different, much rounder NC, showing a $\approx$ 20 nm-sized pore defect within the particle. Scale bars: 20 nm.

Figure S2 shows HR-STEM images of an individual BTO NC oriented relative to the electron beam to yield atomic column resolution (Figure S2b). We do not observe that the NC has

any layer of different crystallographic symmetry than the one at its center. Note that the line crossing the NC from top to bottom on Figure S2a may be either a structural defect or an in-plane domain wall.

Evidence of a phase transition from temperature dependence Raman spectroscopy of BTO nanopowder

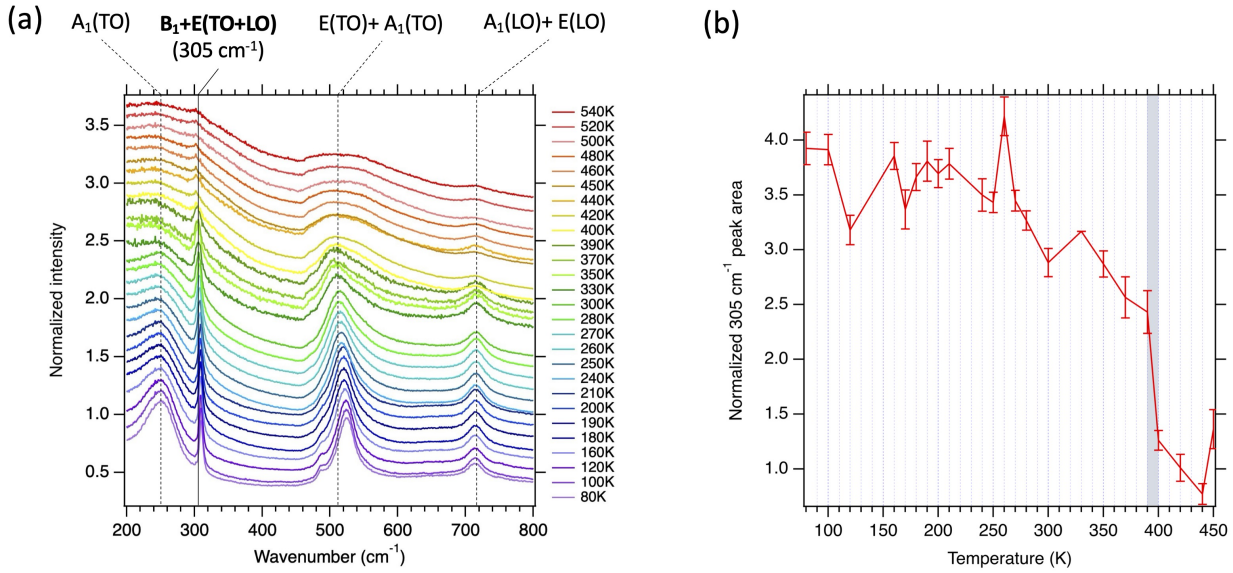

Figure S3: **Temperature dependence of BTO Raman spectrum and Curie temperature estimate**. (a) Raman spectrum of BTO nanopowder at temperatures varying from 80 K to 540 K. In the tetragonal phase (space group P4mm) BTO symmetry belongs to the point group C^1_{4v} which irreducible representation is $\Gamma^{\text{optic}}_{C_{4v}} = 3(A_1 + E) + E + B_1$. Due to long-range electrostatic forces, the A_1 and E modes are further divided into transverse and longitudinal optical modes (LO and TO, respectively[40]). On top of the graph, we identified by their group nomenclature a series of four groups of spectrally not-all-resolved peaks. All spectra were normalized to the ≈ 250 cm^{-1} peak intensity (to account for temperature depopulation), and the spectra were shifted vertically for clarity. (b) Area of the ≈ 305 cm^{-1} normalized peak versus temperature. The shaded zone indicates the range of temperature in which the peak area change most, and from which we infer a phase transition Curie temperature of 395 ± 2 K.

Characterization of BTO nanocrystals bound to the substrate

The NC are attached to the numbered grid with a thin layer of PEDOT:PSS conductive polymer. A layer thickness of ≈ 45 nm was measured by AFM, as shown on Figure S4a,b,

after having removed a tape that had been placed on an edge of the substrate before spin-coating PEDOT:PSS. Similarly, we estimated how much the NC sinks into the PEDOT:PSS before its annealing, by measuring the depth of the hole that remains in the event of the PFM tip drags the NC (Figure S4c,d). We estimate this depth to be $\approx$ 30 nm. The heightened contour encircling the hole is likely to be the concave meniscus that holds the particle, confirming the wetting of the BTO by PEDOT:PSS.

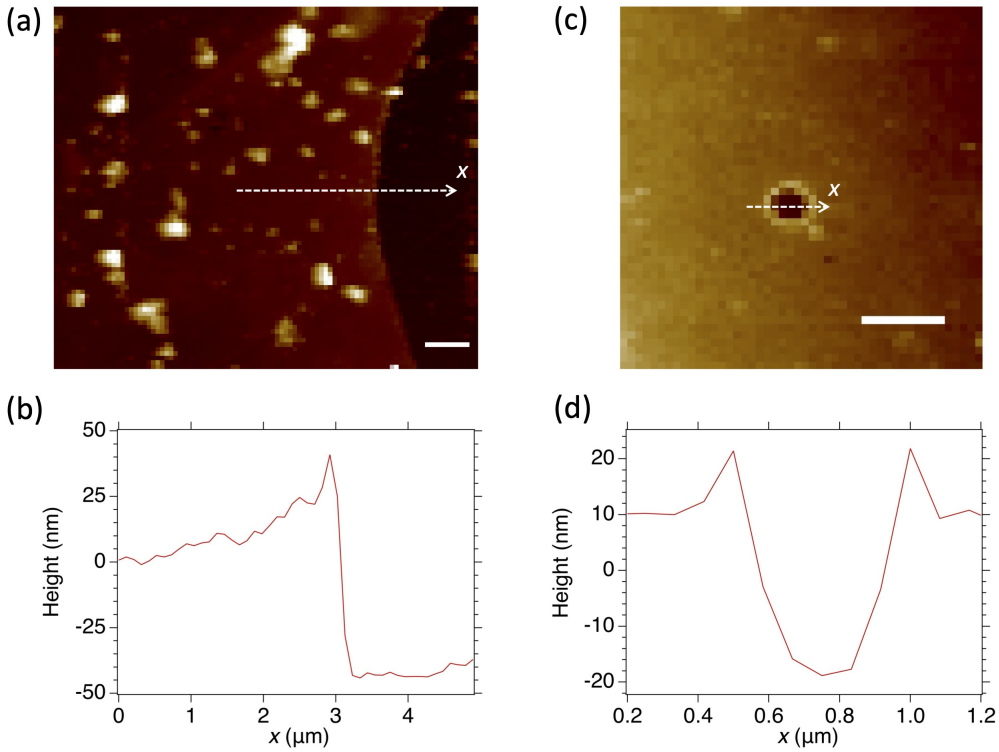

Figure S4: **PEDOT:PSS layer thickness and depth of penetration of NC in the layer**. (a) PEDOT:PSS layer near an edge of the substrate after tape removal. (b) Height profile along the dashed white line in panel (a). (c) Hole in the PEDOT:PSS layer after a NC was dragged by the PFM tip during scanning. (d) Height cross-section along the dashed line of panel (c) showing that the particle was immersed partially in the polymer layer.

The single NC that we studied by PFM were first identified using SEM and their position in the numbered gold grid, as shown on Figure S5a, allowed to retrieve them in PFM.

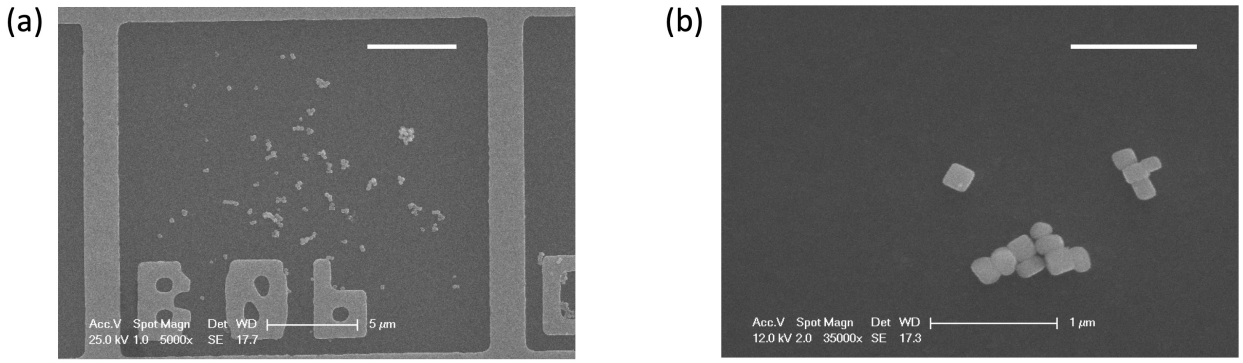

Figure S5: **BTO nanocrystals bound to the numbered gold-made grid**. (a) Large field of view that allows one to read the grid number (here B06). Scale bar: 5 μm. (b) Smaller field of view with an isolated NC candidate in the middle. Scale bar: 1 μm.

For the PFM study, we considered only isolated nanocrystals of close to cubic shape, such as the one in the middle of Figure S5b. Figure S6 shows the size and shape distributions of the isolated NC subsequently studied by PFM.

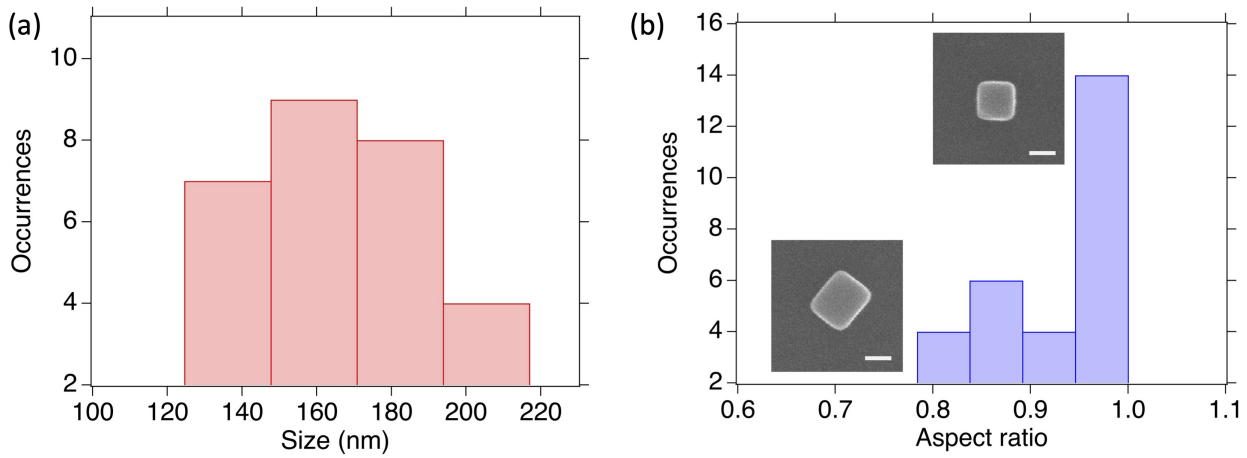

Figure S6: **Size distribution and morphology of the individual BTO nanocrystals spincoated on ITO-coated coverslip**. (a) Distribution of NC size (defined as the mean value of the side length), with an average and standard deviation of 160 ± 28 nm. (b) Aspect ratio of the particles (defined as the size of the short side on the one of the long side), revealing a majority of particles with ratio 1, indicating a close-to-cubic shape. Inset: SEM images of single nanoparticles with aspect ratio 1 and 0.8. Scale bar: 100 nm.

2.2. Evidence of non-electromechanical effects and use of electrostatic blind spot setting to suppress them

We evidenced the existence of non-electromechanical effects in PFM measurements and demonstrated their suppression when the laser spot used to measure the cantilever deflection is placed at an electrostatic blind spot (ESBS) position. This approach was first described in Killgore *et al.*[47]

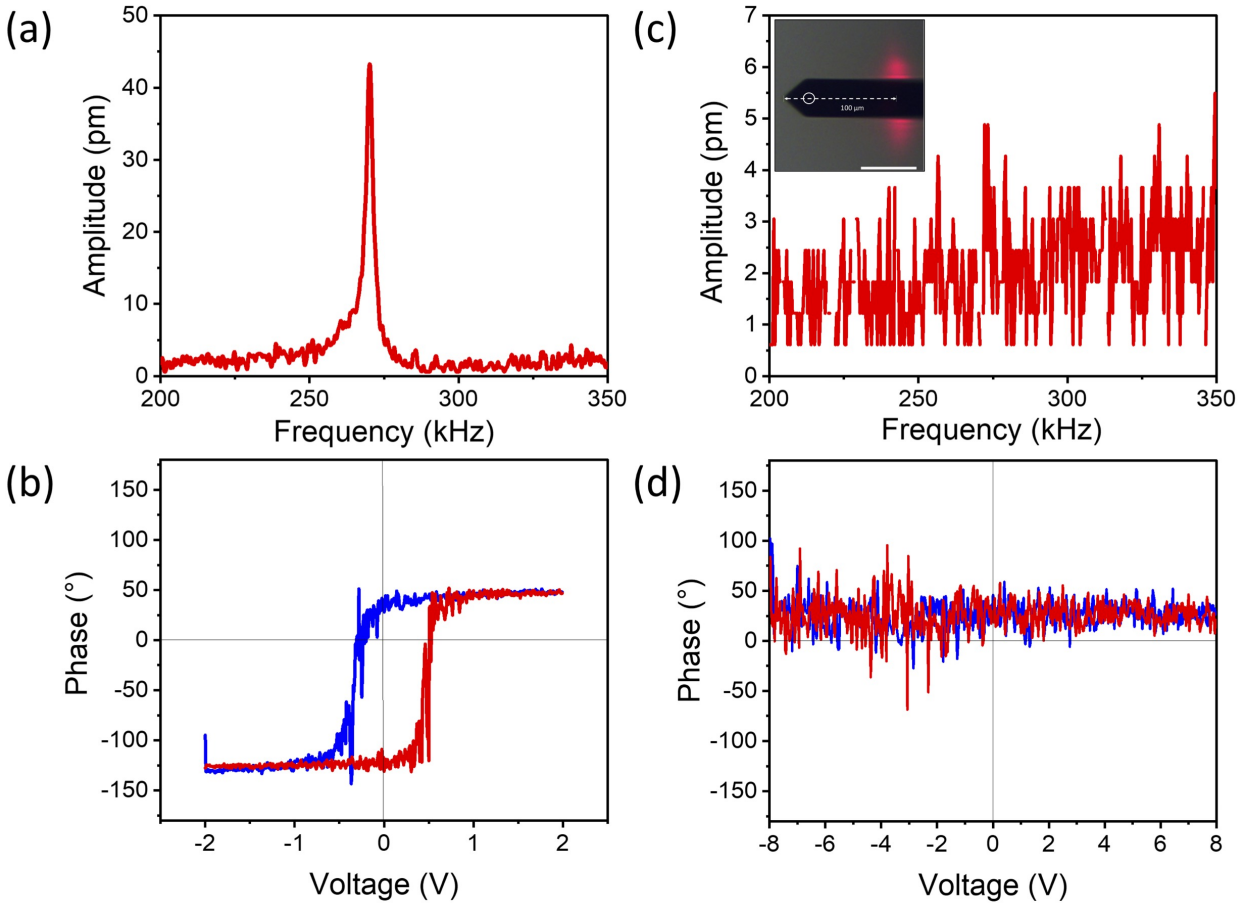

Figure S7: **PFM artifacts and their suppression by finding the ESBS position**. (a,b) When the deflection laser spot is positioned above the tip at the extremity of the cantilever, it induces a contact resonance on ITO in the 220-280 kHz range (a) and an hysteresis loop when ramping a DC bias between +2 V and -2 V (b). (c,d) By moving the laser spot away from the cantilever extremity to the ESBS position, the contact resonance can be suppressed (c) as well as the hysteresis loop (d). Inset of panel (c): picture of ESBS position of the red laser on the cantilever (length $L = 225$ μm) located at 100 μm from the cantilever tip (corresponding to $0.45L$). The conventional laser position is indicated by the white circle. Scale bar: 50 μm.

We first confirmed non-electromechanical effects leading to a PFM signal on an ITO coated substrate alone, with no ferroelectric material deposited on it. These effects were observed through different signatures that were also useful to determine ESBS position by suppressing them in situations where they should not exist, typically on non-ferroelectric materials like in our case the ITO layer. The artifacts observed included the presence of a cantilever contact resonance (Supporting Figure S7a), or a hysteresis loop (Figure S7b), or of a PFM contrast in freshly "written" regions, when the deflection laser spot was adjusted at the extremity of the cantilever, as conventionally done in atomic force microscopy.

As we moved the deflection laser spot further from the cantilever extremity, as shown on the inset picture of Figure S7c, we managed to find a position, the ESBS position, for which the contact resonance disappeared (Figure S7c) and the hysteresis cycle flattened (Figure S7d), removing the previous artifacts.

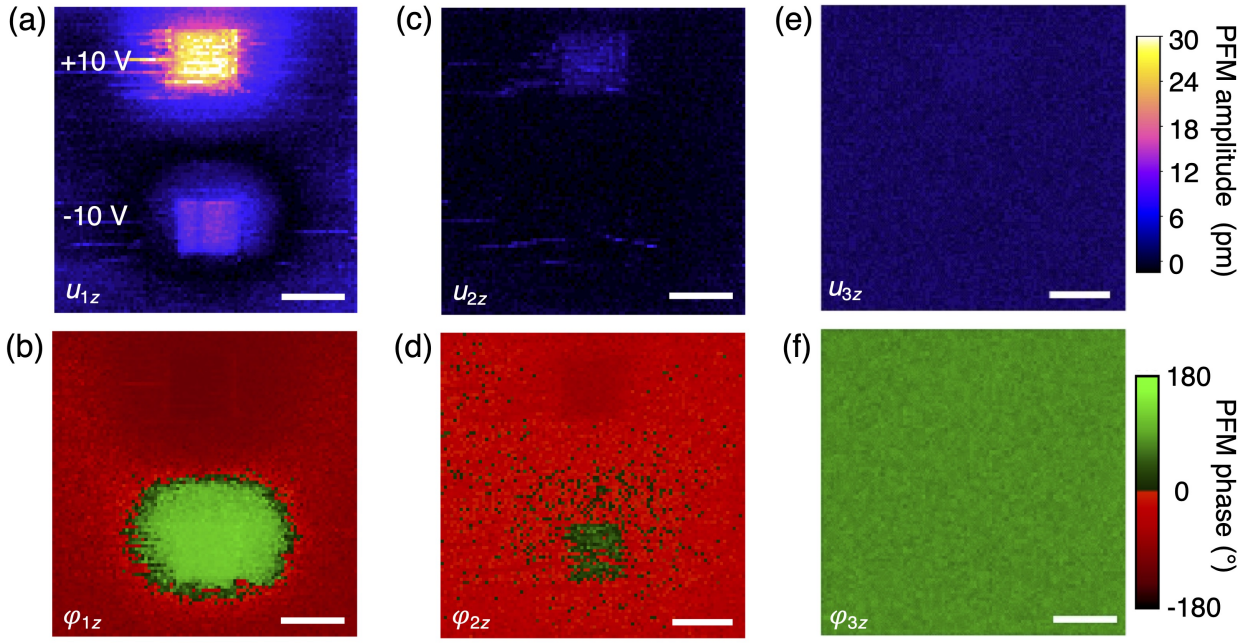

Figure S8: **Suppression of electrostatic cross-talk after adjusting AFM laser spot at ESBS location** (a,b) PFM displacement amplitude and phase maps after writing on ITO with +10 V and -10 V with the laser spot positioned at the cantilever tip. (c,d) Same region with the laser positioned halfway between the ESBS position and the tip. (e,f) Amplitude and phase images of the same region with laser at ESBS positioned approximately 100 μm away from the cantilever tip showing absence of contrast in amplitude and phase. Scale bar: 1 μm.

As mentioned, another type of electrostatic artifact could be detected in PFM phase and amplitude images of ITO surface after having written on a square of 1 μm side with +10 and -10 V potentials. Supporting Figure S8a,b shows PFM images with the deflection laser positioned at the extremity of the cantilever just above the tip. Figure S8c,d shows the same region when the laser was positioned between the tip and the ESBS position, showing a decrease in contrast in phase and amplitude signals. Finally, Figure S8e,f shows PFM amplitude and phase images of the same region when we placed the laser at ESBS position (identified by the disappearance of the contact resonance, like in Figure S7c). The absence of phase and amplitude contrast confirms the suppression of electrostatic parasitic effects in the PFM signal.

2.3. Lateral PFM resonance curve of a cantilever

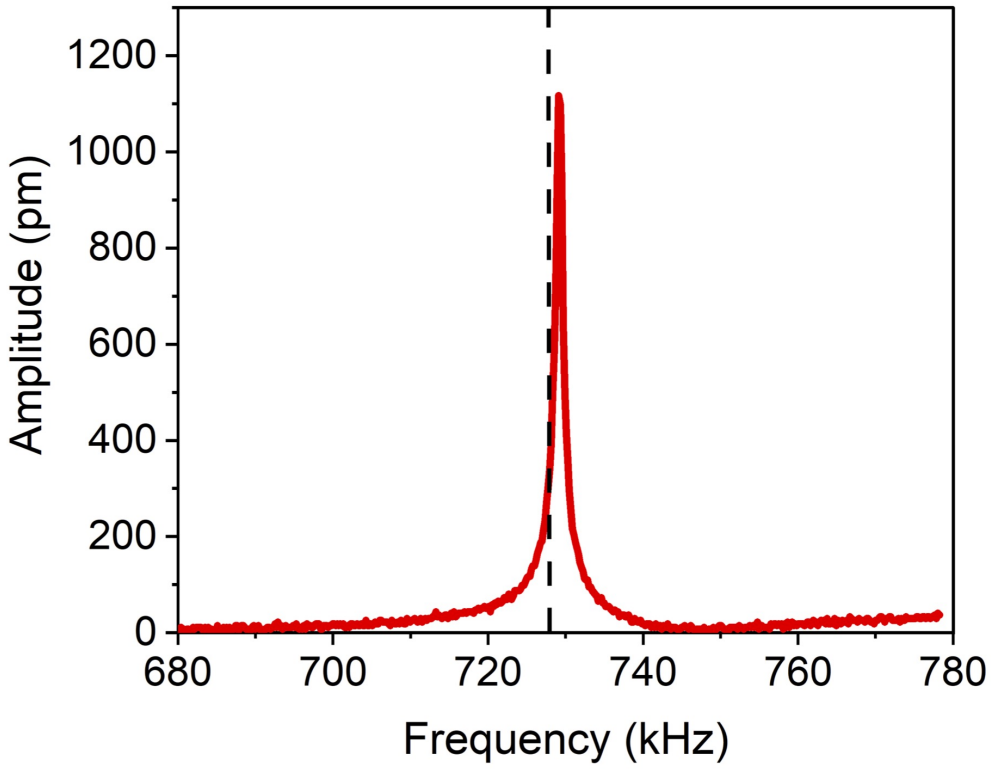

Figure S 9: **In-plane resonance curve at 730 kHz at 1.5 V drive voltage**. PFM imaging was done near the resonance peak at 727.8 kHz, indicated by the black dashed line.

2.4. Lateral PFM mapping of three additional BTO NC

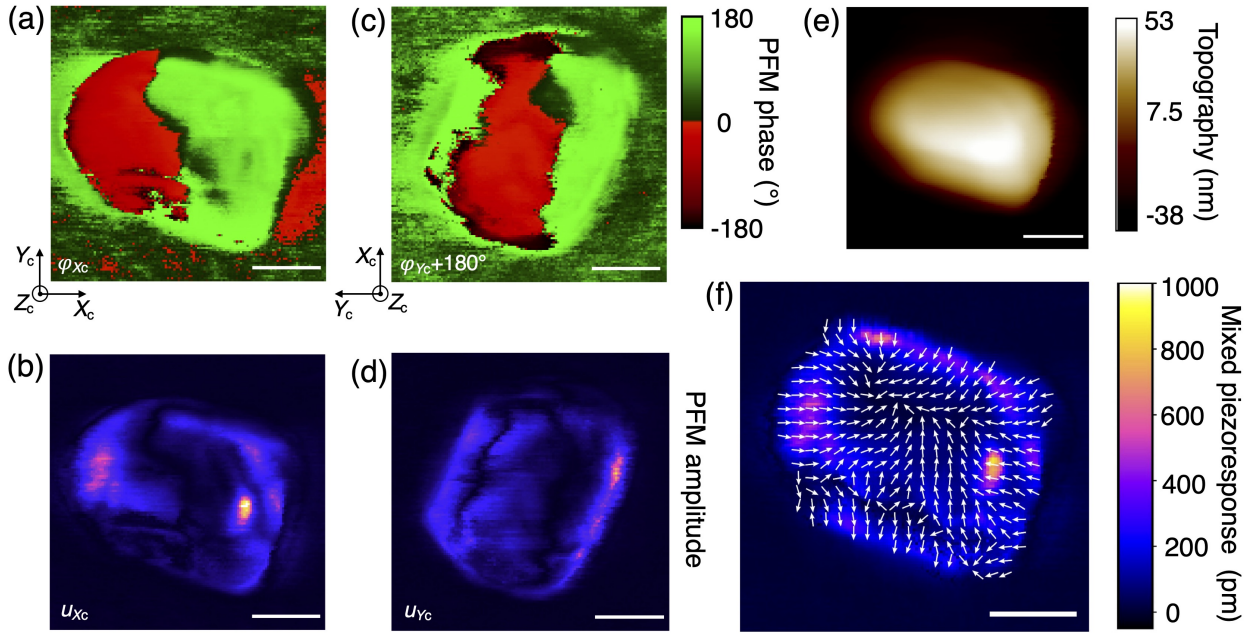

Figure S 10: **Lateral piezoresponse displacement mapping on the single BTO NC#2**. (a,b) Lateral piezoresponse phase φ_x and amplitude u_x along x- axis. (c,d) Lateral piezoresponse phase φ_y and amplitude u_y along the y- axis (sample rotated counterclockwise). (e) Topography image of the particle. (f) Mixed lateral piezoresponse field $\boldsymbol{u}^{\mathrm{m}}(u_{X_\mathrm{c}}\cos(\varphi_{X_\mathrm{c}}-\varphi_{\mathrm{offset}}), u_{Y_\mathrm{c}}\cos(\varphi_{Y_\mathrm{c}}-\varphi_{\mathrm{offset}}))$, with $\varphi_{\mathrm{offset}} = 34°$, displayed by superimposed norm maps (color code) and direction (array of fixed-length arrows at nodes of a 7.8 nm pitch grid). Scale bars (all scans): 50 nm.

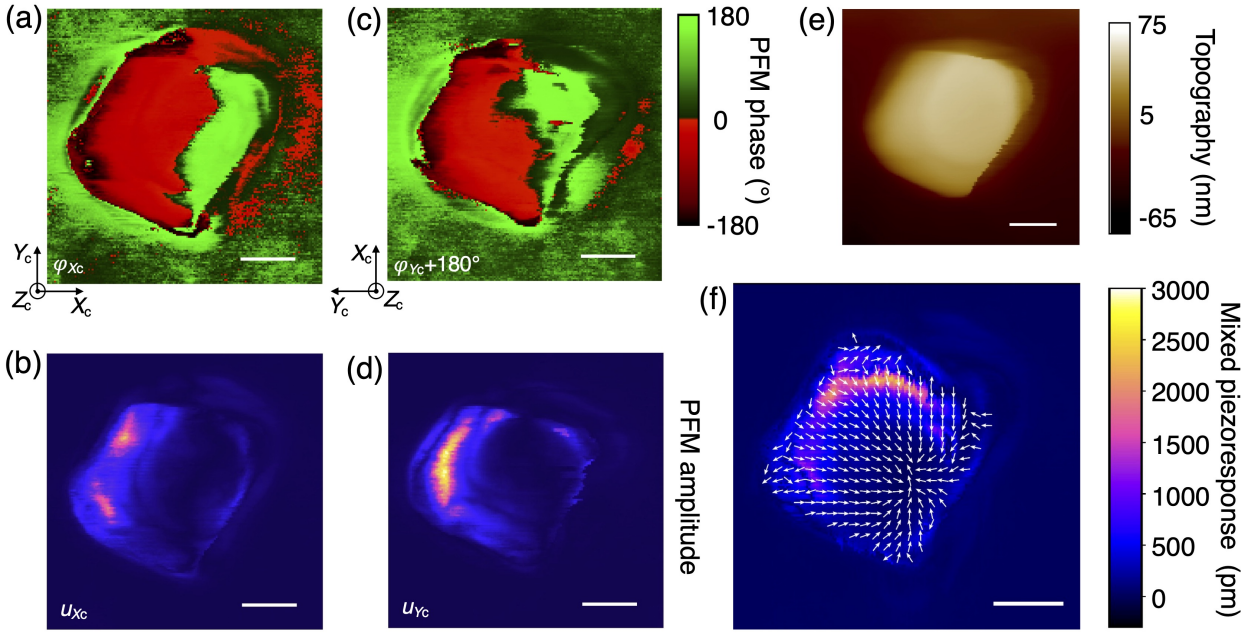

Figure S 11: **Lateral piezoresponse displacement mapping on the single BTO NC#3**. (a,b) Lateral piezoresponse phase φ_x and amplitude u_x along x- axis. (c,d) Lateral piezoresponse phase φ_y and amplitude u_y along y- axis (Sample rotated counter-clockwise. (e) Topography image of the particle. (f) Mixed lateral piezoresponse field $\boldsymbol{u}^{\mathrm{m}}(u_{X_\mathrm{c}}\cos(\varphi_{X_\mathrm{c}}-\varphi_{\mathrm{offset}}), u_{Y_\mathrm{c}}\cos(\varphi_{Y_\mathrm{c}}-\varphi_{\mathrm{offset}}))$ with $\varphi_{\mathrm{offset}} = 20°$, displayed by superimposed maps of norm (color code) and direction (array of fixed-length arrows at nodes of a 7.8 nm pitch grid). Scale bars (all scans): 50 nm.

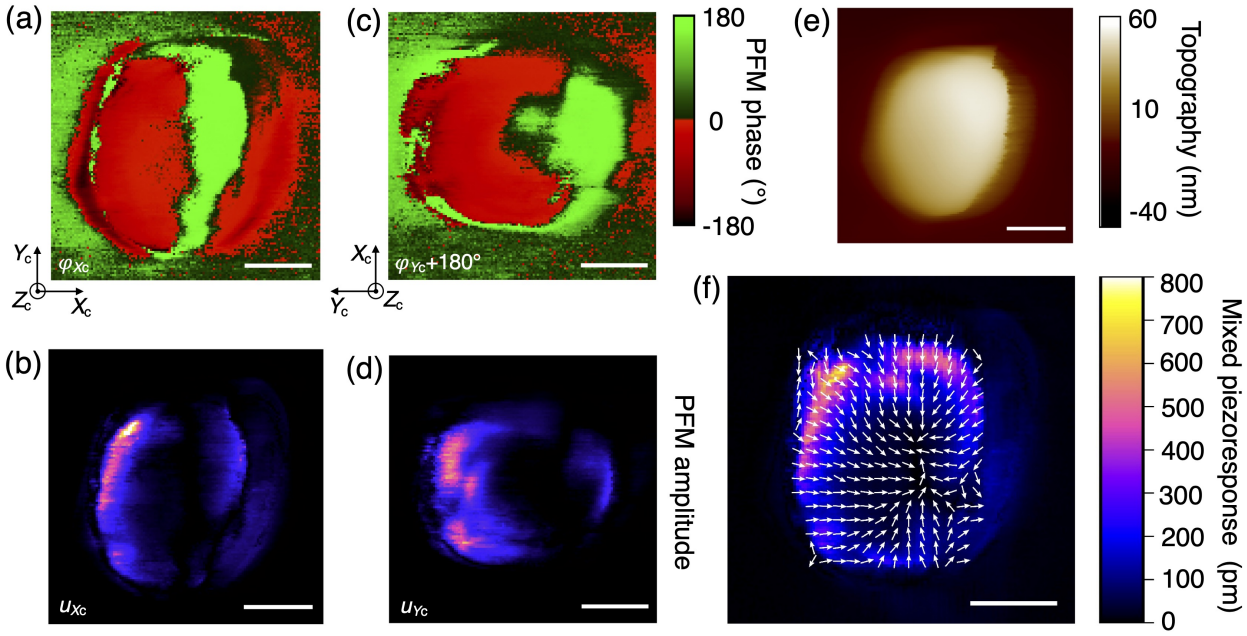

Figure S 12: **Lateral piezoresponse displacement mapping on the single BTO NC#4.** (a,b) Lateral piezoresponse phase φ_x and amplitude u_x along x- axis. (c,d) Lateral piezoresponse phase φ_y and amplitude u_y along y- axis (Sample rotated counter-clockwise. (e) Topography image of the particle. (f) Mixed lateral piezoresponse field $\boldsymbol{u}^{\mathrm{m}}(u_{X_\mathrm{c}}\cos(\varphi_{X_\mathrm{c}} - \varphi_{\mathrm{offset}}), u_{Y_\mathrm{c}}\cos(\varphi_{Y_\mathrm{c}} - \varphi_{\mathrm{offset}}))$, with $\varphi_{\mathrm{offset}} = 15°$, displayed by superimposed maps of norm (color code) and direction (array of fixed-length arrows at nodes of a 7.8 nm pitch grid). Scale bars (all scans): 50 nm.

2.5. Additional data on phase field simulations

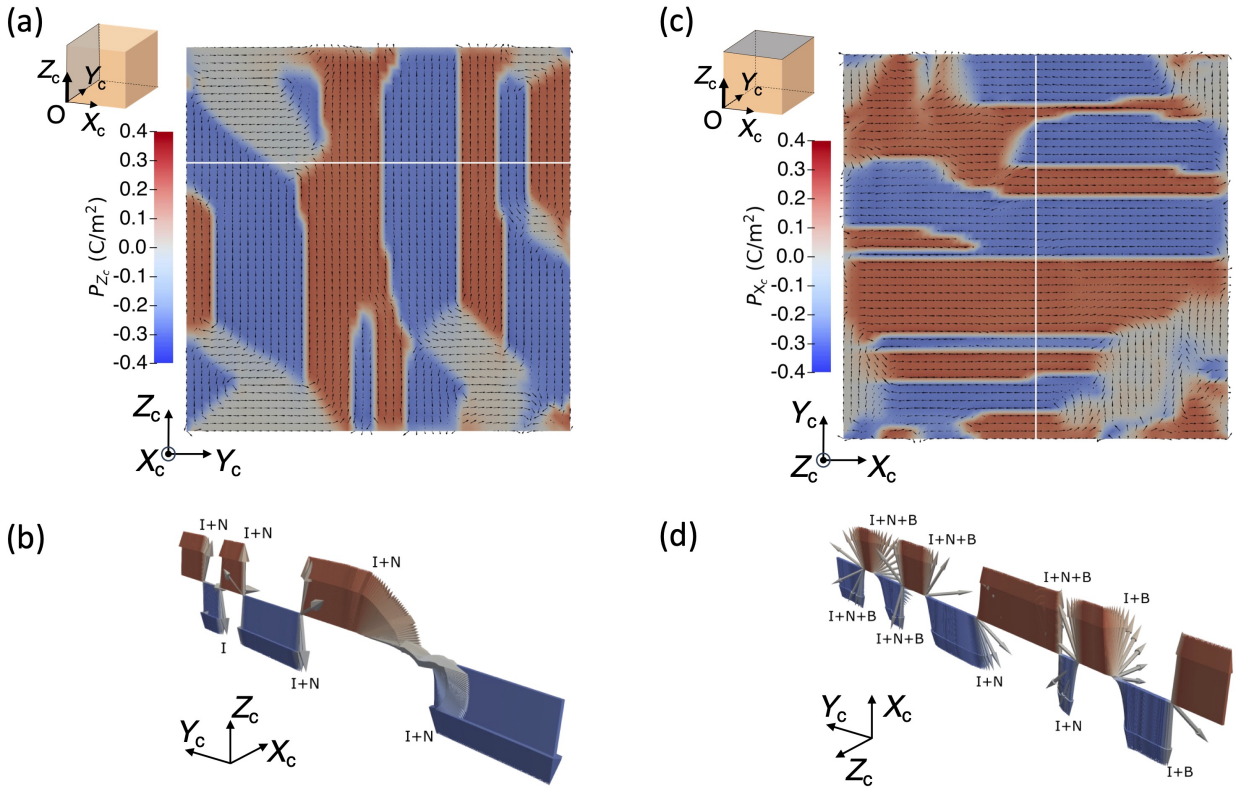

Figure S 13: **Distribution of polarization in facets parallel or orthogonal to the polar axis, and illustration of the type of domain walls they host**. (a) The distribution of polarization on facet (Y_cOZ_c) at $X_c = 0$ nm shows the presence of $\pm Z_c$-oriented domains with $\pm Y_c$ domains near the surfaces. (b) Three-dimensional representation of the direction of the polarization vector $\boldsymbol{P}/|\boldsymbol{P}|$ showing the partial Néel nature of the walls of the predominantly Ising domain along the line $(X_c = 0 \text{ nm}, Y_c, Z_c = -71 \text{ nm})$. (c) The distribution of polarization on the $Z_c = 100$ nm top facet shows a predominantly $\pm X_c$ oriented polar domain (red and blue) with some $\pm Y_c$ oriented domains (gray). (d) Three-dimensional representation of the direction of the polarization vector showing that the domain walls along the line $(X_c = 50 \text{ nm}, Y_c, Z_c = 100 \text{ nm})$ present the partial Néel or/and Bloch character of the main Ising domain walls.

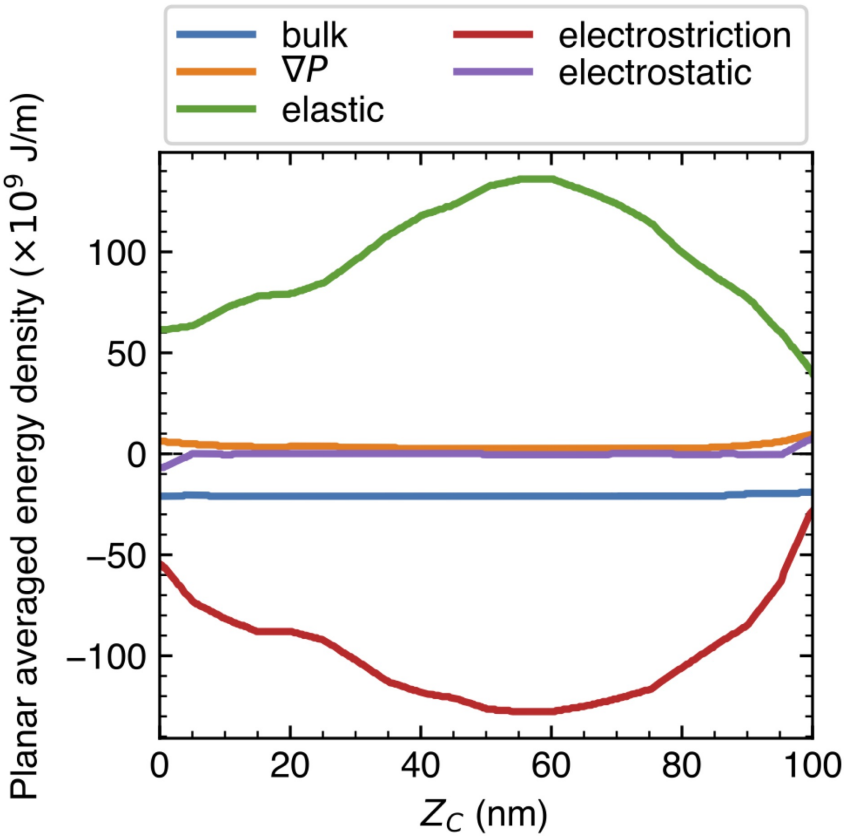

Figure S14: **Distribution of the different components of the energy density across a nanocrystal**. Planar averaged energy density contributions showing the bulk energy density (blue), the gradient of polarization energy density (orange), the elastic energy density (green), the electrostatic energy density (purple) and electromechanical energy density (red). Energy densities are averaged in planes perpendicular to the main polar axis Z_c.